nature communications

Article

https://doi.org/10.1038/s41467-024-52326-1

# SHANK3 depletion leads to ERK signalling overdose and cell death in KRAS-mutant cancers

Received: 9 December 2022

Accepted: 3 September 2024

Published online: 12 September 2024

Check for updates

Johanna Lilja[1,18], Jasmin Kaivola[1,18], James R. W. Conway[1], Joni Vuorio[2], Hanna Parkkola[1], Pekka Roivas[1,3], Michal Dibus[1], Megan R. Chastney[1], Taru Varila[1], Guillaume Jacquemet[1,4,5,6], Emilia Peuhu[1,7], Emily Wang[8], Ulla Pentikäinen[1,3], Itziar Martinez D. Posada[1], Hellyeh Hamidi[1], Arafath K. Najumudeen[9,10], Owen J. Sansom[10,11], Igor L. Barsukov[8], Daniel Abankwa[1,12], Ilpo Vattulainen[2], Marko Salmi[3,13,14] & Johanna Ivaska[1,14,15,16,17]

The *KRAS* oncogene drives many common and highly fatal malignancies. These include pancreatic, lung, and colorectal cancer, where various activating *KRAS* mutations have made the development of KRAS inhibitors difficult. Here we identify the scaffold protein SH3 and multiple ankyrin repeat domain 3 (SHANK3) as a RAS interactor that binds active KRAS, including mutant forms, competes with RAF and limits oncogenic KRAS downstream signalling, maintaining mitogen-activated protein kinase/extracellular signal-regulated kinase (MAPK/ERK) activity at an optimal level. SHANK3 depletion breaches this threshold, triggering MAPK/ERK signalling hyperactivation and MAPK/ERK-dependent cell death in *KRAS*-mutant cancers. Targeting this vulnerability through RNA interference or nanobody-mediated disruption of the SHANK3–KRAS interaction constrains tumour growth in vivo in female mice. Thus, inhibition of SHANK3–KRAS interaction represents an alternative strategy for selective killing of *KRAS*-mutant cancer cells through excessive signalling.

Aberrant KRAS activity has been identified in >20% of *human* cancers[1] with a substantially higher incidence in some of the most inherently therapy-resistant cancer types, including non-small cell lung cancers (NSCLC; 30% incidence), colorectal cancer (CRC; 50% incidence), and pancreatic ductal adenocarcinoma (PDAC; 95% incidence)[1,2]. Oncogenic mutations in *KRAS* induce the constitutive activation of proliferative signalling cascades, promoting cancer progression and conferring resistance to standard-of-care

[1]Turku Bioscience Centre, University of Turku, FI-20520 Turku, Finland. [2]Department of Physics, University of Helsinki, Helsinki, Finland. [3]Institute of Biomedicine, University of Turku, FI-20520 Turku, Finland. [4]Faculty of Science and Engineering, Cell Biology, Åbo Akademi University, FI-20520 Turku, Finland. [5]Turku Bioimaging, University of Turku and Åbo Akademi University, FI-20520 Turku, Finland. [6]InFLAMES Research Flagship Center, Åbo Akademi University, FI-20520 Turku, Finland. [7]Institute of Biomedicine, Cancer Research Laboratory FICAN West, University of Turku, FI-20520 Turku, Finland. [8]Institute of Systems, Molecular and Integrative Biology, University of Liverpool, Liverpool, UK. [9]Institute of Biotechnology, HiLIFE, University of Helsinki, Helsinki, Finland. [10]CRUK Scotland Institute, Garscube Estate, Switchback Road, Glasgow G61 1BD, UK. [11]Institute of Cancer Sciences, University of Glasgow, Garscube Estate, Switchback Road, Glasgow G61 1QH, UK. [12]Department of Life Sciences and Medicine, University of Luxembourg, 4365 Esch- sur-Alzette, Luxembourg. [13]MediCity Research Laboratory, University of Turku, FI-20520 Turku, Finland. [14]InFLAMES Research Flagship Center, University of Turku, FI-20520 Turku, Finland. [15]Department of Life Technologies, University of Turku, Turku, Finland. [16]Foundation for the Finnish Cancer Institute, Tukholmankatu 8, FI-00014 Helsinki, Finland. [17]Western Finnish Cancer Center, University of Turku, Turku FI-20520, Finland. [18]These authors contributed equally: Johanna Lilja, Jasmin Kaivola. e-mail: Johanna.ivaska@utu.fi

treatments[3–5]. Unfortunately, the survival of patients with *KRAS*-mutated NSCLC or PDAC has barely improved over the past few decades[6], highlighting the urgent need to broaden our view on targeting oncogenic KRAS.

KRAS is a plasma membrane-associated small GTPase, active in its GTP-bound form and inactive in its GDP-bound state[7]. Active KRAS interaction with its effector RAF switches on downstream pathways such as the mitogen-activated protein kinase (MAPK)/extracellular signal-regulated kinase (ERK) signalling axis, triggering a pro-survival response in cancer cells through transcription factors that promote cell growth[8,9]. Given the central role of oncogenic KRAS as a driver mutation in many cancer types, pharmacological inhibition of KRAS has been a major research area for decades. Through the accrued knowledge of the structural and biochemical characteristics of different KRAS mutants, the field has seen a recent development of mutation-specific drugs with promising preclinical and clinical efficacy[10–18]. The only approved allele-specific inhibitors target KRASG12C, a mutation found in ~12% of all *KRAS*-driven tumours[11–16,19,20], leaving ~88% of patients without a KRAS-targeted treatment option. In addition, various resistance mechanisms have already been reported, indicating significant limitations of mutation-specific inhibitors in heterogeneous tumours[21–23]. To address a broader patient population, vast efforts are being made in several new pan-KRAS approaches targeting all KRAS mutants[10,24,25]. These include pharmacological manipulation of KRAS upstream activators, such as SHP2 and SOS1[26–28], and attempts to develop pan-KRAS protein degradation strategies, such as proteolysis-targeting chimeras (PROTACs)[29]. These Pan-KRAS inhibitors hold promise for patients for whom targeted therapy remains elusive.

A common precision medicine approach has been to treat cancer by inhibiting specific oncogenic mutations or pathways. Recently, however, deliberate MAPK/ERK pathway hyperactivation by ERK2 overexpression or inhibition of ERK phosphatases DUSP4 and 6 was shown to reduce NRAS and BRAF mutant cell viability[30–32] and a gain-of-function oncogene activation screen demonstrated that hyperactivation of oncogenic pathways can trigger context-specific lethality across cancer cell lines[33].

We and others previously showed that the multidomain scaffold protein SH3 and multiple ankyrin repeat domain 3 (SHANK3) adopts a RAS-association (RA) domain-like fold, within its N-terminal Shank/ProSAP (SPN) domain, with high affinity for GTP-bound RAS and Rap small GTPases[34,35]. SHANK3 was initially identified in the excitatory synapses of the central nervous system[36]. We discovered that SHANK3 functions beyond the nervous system, regulating the cell cytoskeleton[37] and cell adhesion by binding to Rap1 and inhibiting the formation of an integrin-activating complex in non-neuronal cells and cancer cells[34]. However, whether SHANK3 plays a functional role in oncogenic RAS signalling remains unknown.

In this work, we identify SHANK3 as a RAS interactor that competes with RAF for binding to active KRAS. We show that this functionally limits oncogenic MAPK/ERK signalling to an optimal level for *KRAS*-mutant cancer cell growth. We further demonstrate that SHANK3 depletion results in hyperactivation of this pathway, leading to cancer cell death by signalling overdose in *KRAS*-mutant cancers with different *KRAS* mutations. Our data demonstrate that SHANK3 depletion impairs the growth of pre-existing *KRAS*-mutant tumours, highlighting the possibility of SHANK3 targeting as a potential actionable cancer dependency. We provide proof-of-concept evidence that SHANK3 can be targeted by developing nanobodies disrupting the SHANK3–KRAS protein-protein interaction. We demonstrate the efficacy of these nanobodies in inducing apoptosis in *KRAS*-mutant cancers. Collectively our data reveal that the SHANK3–KRAS interaction is an exploitable vulnerability of pan-*KRAS*-driven cancers.

## Results

### SHANK3 depletion impairs cell proliferation in a panel of KRAS-mutant cancer cell lines

To investigate the role of SHANK3 in cancer cell viability, we depleted endogenous SHANK3 using two unique RNA interference (RNAi) oligonucleotides (siSHANK3_2 and siSHANK3_7) in a large panel of *human* PDAC, NSCLC and CRC cell lines harbouring either distinct *KRAS* mutations or wild-type (WT) *KRAS* (Fig. 1a and silencing validated in Supplementary Fig. 1a). Cell proliferation was strongly impaired with both *SHANK3* siRNAs in each of the 12 tested cancer cell lines with activating mutations in *KRAS* [mean inhibition of proliferation (%): 63.3 ± 4.4% (PANC-1), 66.1 ± 5.6% (Panc10.05), 38.9 ± 4.2% (AsPC-1), 63.0 ± 19.6% (Su86.86), 55.5 ± 4.7% (SW1990), 55.5 ± 8.8% (YAPC), 74.5 ± 4.6% (PaTu8902), 79.5 ± 19.1% (MIA PaCa-2), 50.8 ± 20.5% (A549), 72.1 ± 7.5% (H441), 38.0 ± 22.1% (HCT-15), 81.3 ± 8.6% (HCT-116)] (Fig. 1a). In contrast, the cancer cell lines harbouring WT *KRAS* did not show consistent and/or significant inhibition of proliferation following SHANK3 depletion with the two *SHANK3* siRNA [mean inhibition of proliferation (%): -3.9 ± 33.2% (H292), 14.0 ± 20.9% (H226), 13.6 ± 8.0% (HT-29), 27.9 ± 21.6 (BxPC3) and 0.4 ± 2.5 (ARPE)] (Fig. 1a). Interestingly, the pan-cancer Broad and Sanger knock-out cancer cell line viability screens did not include guide RNAs or shRNA against *SHANK3*, suggesting that our current view of genes essential for cancer survival may be lacking some more important regulators[38,39]. Our data thus indicate that *SHANK3* depletion, while dramatically affecting *KRAS*-mutant cell proliferation, has no or marginal effects on WT *KRAS* cells.

The growth of *KRAS*-mutant pancreatic (PANC-1) and lung cancer (A549) cell colonies was also reduced by ~90% after acute *SHANK3* silencing with the two independent siRNAs (Supplementary Fig. 1b). Similarly, in a 3-dimensional (3D) setting, the growth of *KRAS*-mutant pancreatic (PANC-1 and AsPC-1) and lung (A549) cancer spheroids was also significantly inhibited (Fig. 1b and Supplementary Fig. 1c).

To examine if SHANK3 is also essential for tumorigenesis, we established pancreatic and lung cancer xenograft models on chick embryo chorioallantoic membranes (CAMs) in fertilised eggs (Supplementary Fig. 1d). In line with our in vitro results, we observed a significant decrease in both tumour weight and the number of proliferating cells, as indicated by Ki-67 staining, in *SHANK3*-silenced *KRAS*-driven PANC-1 and A549 xenografts (Fig. 1c–e), but not in WT *KRAS* BxPC3 tumours (Supplementary Fig. 1e–g).

These data collectively indicate that the depletion of endogenous SHANK3 effectively blocks cell proliferation and growth in vitro and in vivo in different cancer types driven by distinct *KRAS* mutations.

### SHANK3 interacts specifically with active KRAS to regulate KRAS-mutant cell survival

We had previously determined the crystal structure of the SHANK3 N-terminus, revealing an RA domain-like structure in the SPN domain (Fig. 2a)[34]. A subsequent study elucidated the structure of the SPN domain when bound to HRAS[35]. To understand the role of SHANK3 in regulating *KRAS*-driven tumour growth, we first explored the SHANK3–KRAS interaction. Microscale thermophoresis (MST) and isothermal titration calorimetry (ITC) measurements with purified recombinant proteins indicated that the N-terminal SHANK3 SPN domain alone and the SPN-ARR fragment (comprising the two adjacent N-terminal domains) (Fig. 2a) interact with active (GMPPCP-form) KRAS mutants with similar affinities (Kd = 5.0 ± 0.6 μM for G12V with SPN; and Kd = 5.4 ± 0.7 μM for Q61H with SPN-ARR; Fig. 2b, c and Supplementary Fig. 2a–d). Inactive (GDP-bound) KRAS showed no interaction with SHANK3 SPN-ARR in ITC measurements (Fig. 2d), indicating that the interactions were specific to GTP-bound KRAS. These data show direct SHANK3 SPN domain interaction with KRAS at low micromolar affinity that is dependent on KRAS activity, similar to established RA domain-containing proteins[40].

https://doi.org/10.1038/s41467-024-52326-1

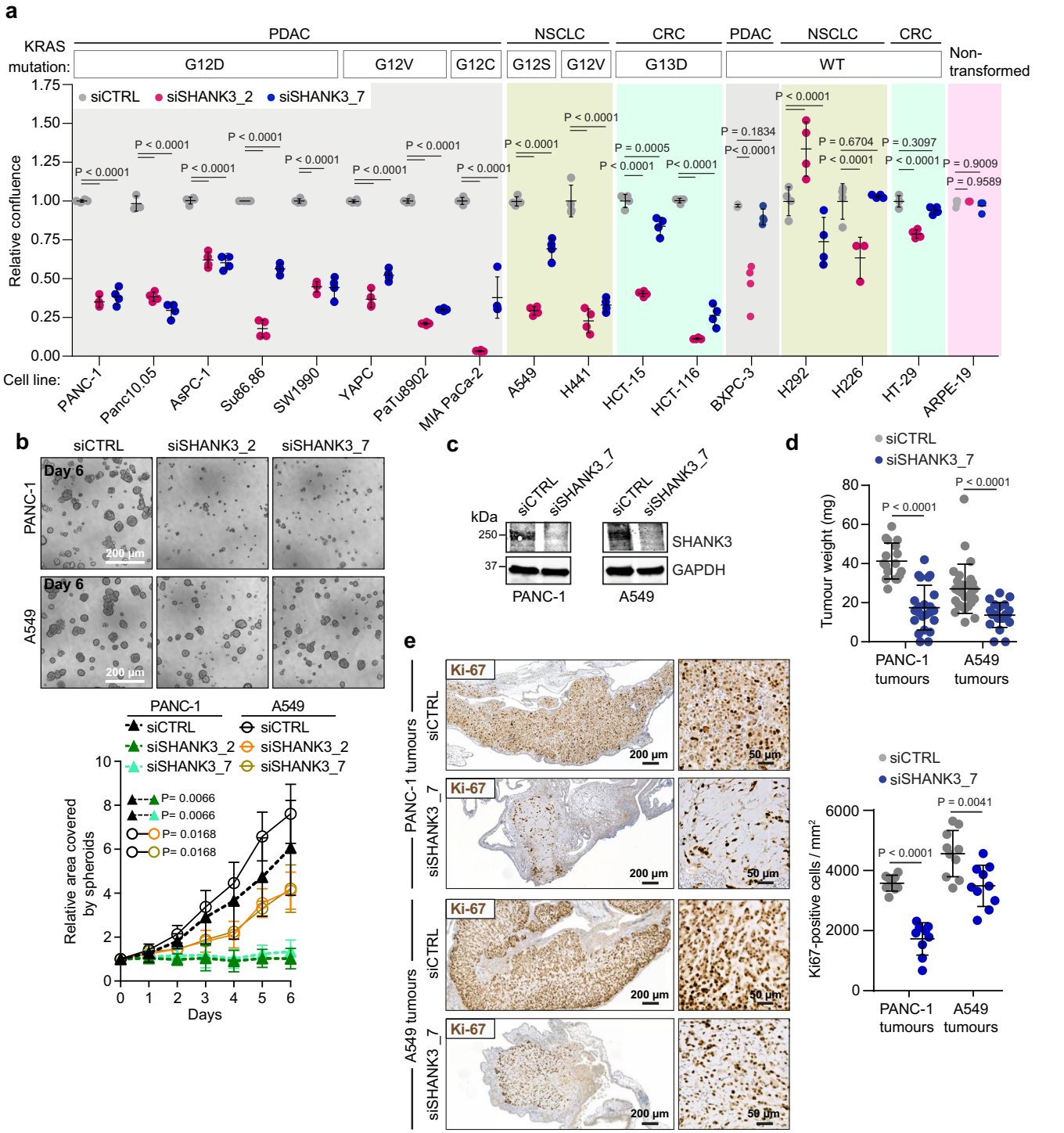


**Fig. 1 | SHANK3 depletion inhibits cell proliferation in vitro and in vivo in different cancer types driven by distinct *KRAS* mutations. a** A cell proliferation screen following control (siCTRL, grey) or *SHANK3* silencing (siSHANK3_2 (red) or siSHANK3_7 (blue)) in wild-type (WT) or *KRAS*-mutant pancreatic (PDAC), lung (NSCLC) and colorectal (CRC) cancer cell lines. ARPE-19, non-transformed retinal epithelial cells. Shown are the individual data points relative to control [the mean of the control is set to 1.0 by definition; data are mean ± s.d.; $n = 3$ (Panc10.05 siCTRL and H226 siSHANK3_2) or 4 (other samples) individually silenced wells; two-way ANOVA with Dunnett's multiple comparisons test]. **b** Spheroid growth of siCTRL or siSHANK3 PANC-1 or A549 cells. Shown are representative images and quantification of spheroid area (mean ± s.d.; $n = 3$ independent experiments; statistical analysis at end point, one-way ANOVA with Holm-Sidak's multiple comparison test). **c**–**e** Analysis of siCTRL or siSHANK3 PANC-1 and A549 tumour growth on chorioallantoic membranes (CAMs). **c** Immunoblots showing SHANK3 protein levels in cell suspensions inoculated onto the CAMs [$n = 1$ (PANC1) and 2 (A549) independent experiments], (**d**) tumour weights, and (**e**) representative immunostainings and quantification of Ki-67-positive cells in tumours. Shown are individual data points [mean ± s.d.; $n = 17$ (PANC-1 siCTRL), 23 (PANC-1 siSHANK3), 27 (A549 siCTRL) or 22 (A549 siSHANK3) (**d**) and 9 (PANC-1) or 10 (A549) (**e**) tumours per sample group from 1 (PANC-1) or 2 (A549) independent experiments; two-way ANOVA with Mann–Whitney test (**d**) and Unpaired two-tailed Student's *t*-test with Welch's correction (**e**)]. Source data are provided as a Source Data file.

https://doi.org/10.1038/s41467-024-52326-1

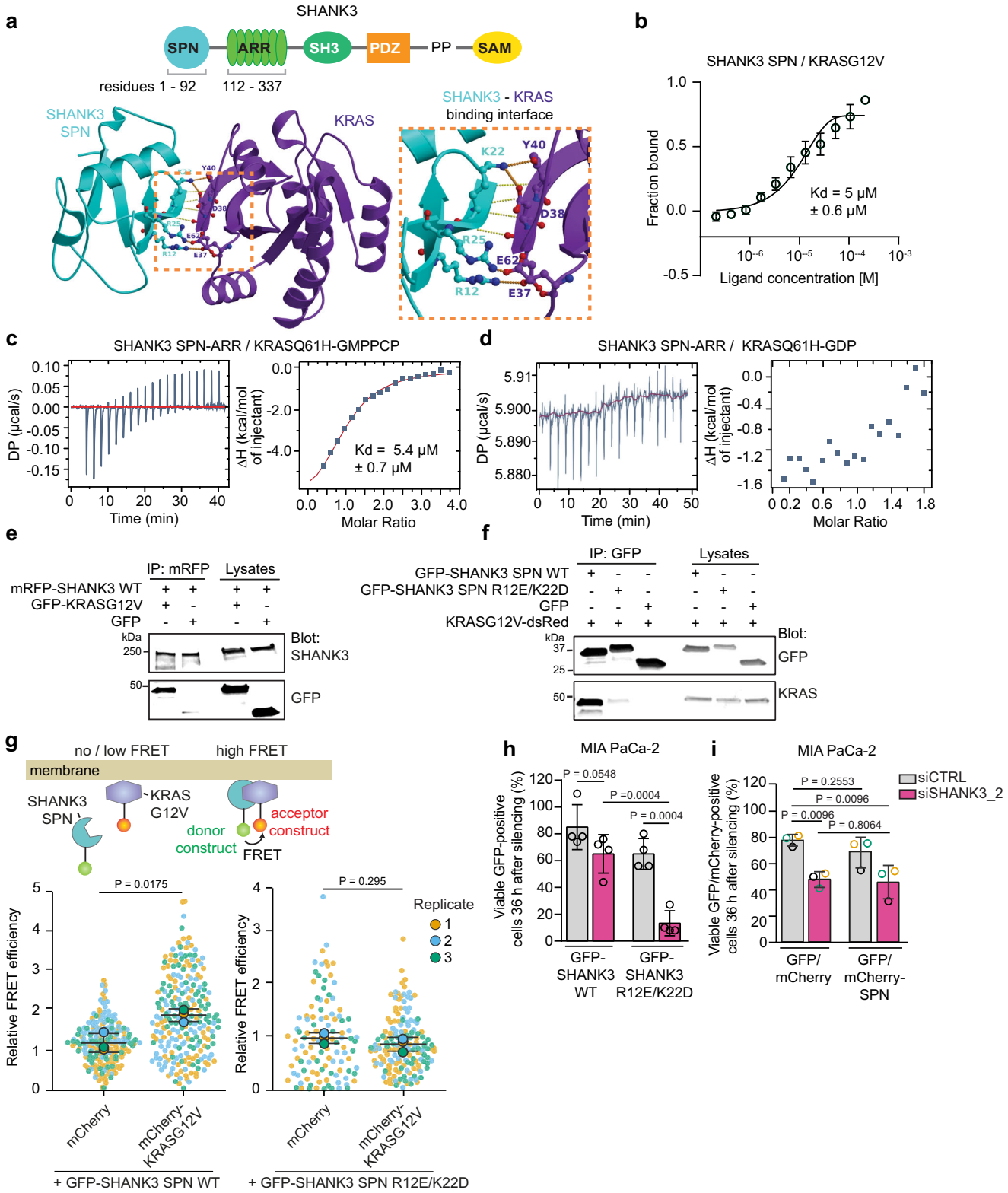


To validate the SHANK3–KRAS protein-protein interaction in cells, we expressed fluorescently tagged KRASG12V and full-length SHANK3 and performed pull-down experiments. Immunoblotting analyses showed that KRASG12V co-immunoprecipitates with the full-length SHANK3 from cell lysates (Fig. 2e). Unfortunately, due to the lack of suitable reagents, we were unable to test endogenous SHANK3 and KRAS binding with co-immunoprecipitation. Based on its crystal structure[34,35], the SHANK3 SPN domain contains the characteristic positively charged RAS-recognizing residues, R12 and K22, which are optimally positioned to form salt-bridges with the E37 and D38/Y40 residues of the KRAS Switch I region (residues from D30 to Y40; Fig. 2a). To analyse the interaction specificity between SHANK3 and KRAS, we introduced charge-reversing mutations into the R12 and K22 residues of the SPN domain (R12E/K22D) and co-expressed the-SHANK3 SPN domains (WT or SPN R12E/K22D mutant) with KRASG12V in cells. Pull-down analyses showed KRASG12V co-

**Fig. 2 | SHANK3 directly interacts with active KRAS, regardless of the activating mutation. a** Schematic of the SHANK3 protein domains and crystal structure model of the SHANK3 SPN domain in complex with active KRAS. The zoom-in shows the critical interacting amino acids. Modified from our previous publication[34]. SPN, Shank/ProSAP N-terminal domain; ARR, ankyrin repeat domain; SH3, Src homology 3 domain; PDZ, PSD-95/Discs large/ZO-1 domain; PP, proline-rich region; SAM, sterile alpha motif domain. **b** MST binding curve for the indicated proteins. The affinity curve and *Kd*-value are obtained from triplicate measurements (mean ± s.e.m.; representative of two independent experiments). **c**, **d** ITC titration and isotherms for interaction between the indicated proteins. Solid line in c indicates fitting to the single-site-bin ding model at 25 °C with 350 μM of KRASQ61H and 20 μM of SPN-ARR (graphs are a representative of three technical replicates; one independent experiment). **e** Immunoprecipitation (IP) in HEK293 cells co-expressing mRFP-SHANK3 WT and GFP-KRASG12V using mRFP-trap beads. A representative western blot is shown (three independent experiments). **f** IP in HEK293 cells co-expressing the GFP-tagged SHANK3 SPN domain (WT or RAS-binding-deficient mutant, R12E/K22D) and KRASG12V-dsRed using GFP-trap beads. A representative western blot is shown (three independent experiments). **g** FRET assay between GFP-tagged SHANK3 SPN domain (WT or R12E/K22D; FRET donor) and mCherry-KRASG12V (FRET acceptor) in HEK293 cells. Quantification of relative FRET efficiency, normalised to mCherry control vector (see methods). Individual data points and the population average of each biological replicate are shown [mean ± s.d.; three independent experiments; unpaired two-tailed Student's *t*-test with Welch's correction; 190 (mCherry + WT SPN), 227 (mCherry-KRASG12V + WT SPN), 108 (mCherry + R12E/K22D SPN), 153 (mCherry-KRASG12V + R12E/K22D SPN) individual data points analysed]. **h**, **i** Rescue of cell viability after *SHANK3* silencing. Quantification of viable GFP- or mCherry-positive MIA PaCa-2 cells expressing either full-length GFP-SHANK3 WT or mutant R12E/K22D (**h**), or GFP/mCherry-tagged SHANK3 SPN domain (**i**) after endogenous *SHANK3* silencing (36 h). Shown are individual data points [mean ± s.d., $n = 4$ (**h**) and 3 (**i**) independent experiments (**i**, each replicate is shown in a different colour); one-way ANOVA with Holm-Sidak's multiple comparison test]. Source data are provided as a Source Data file.

immunoprecipitation with SHANK3 SPN WT, an interaction that was abolished with the SPN R12E/K22D double mutant (Fig. 2f). Accordingly, FLIM-FRET (Förster Resonance Energy Transfer by Fluorescence Lifetime Imaging Microscopy) experiments demonstrated a significant increase in FRET efficiency between mCherry-tagged KRASG12V and GFP-tagged SHANK3 SPN WT, but not the SPN R12E/K22D mutant, in line with SHANK3 and KRASG12V protein-protein interaction (Fig. 2g). Taken together, these data demonstrate that SHANK3 directly interacts with active KRAS, independent of the specific KRAS mutation in question, through the conserved R12 and K22 residues, characteristic of a RAS-effector interface[41].

To validate our hypothesis of SHANK3–KRAS interaction-dependent tumour growth, we tested whether re-expression of siRNA-resistant full-length SHANK3 WT or R12E/K22D mutant could rescue the growth inhibitory effect of *SHANK3* silencing. To test this, we chose the *KRAS*-mutant MIA PaCa-2 pancreatic cancer cell line, as these cells were particularly sensitive to *SHANK3* siRNA-induced growth inhibition (Fig. 1a). We found that the re-expression of SHANK3 WT in *SHANK3*-silenced MIA PaCa-2 cells restores cell viability (Fig. 2h). In contrast, the re-expression of the KRAS-interaction-deficient mutant, SHANK3 R12E/K22D (Fig. 2h), or the SHANK3 SPN domain alone (Fig. 2i) failed to rescue the cell death triggered by loss of SHANK3. Thus, an intact KRAS-binding SPN domain in full-length SHANK3 is critical for the ability of SHANK3 to regulate *KRAS*-mutant cell survival.

## SHANK3 competes with RAF for KRAS binding and modulates downstream MAPK/ERK signalling

KRAS association with the plasma membrane and the ability to recruit downstream effectors, such as RAF, are required for active KRAS signalling[2,42]. We observed that GFP-SHANK3 and endogenous SHANK3 localise to the plasma membrane (Supplementary Fig. 3a), and that GFP-SHANK3 localization overlapped with mutant mCherry-KRASG12V at the membrane (Fig. 3a), prompting us to investigate the possibility of SHANK3 interacting with KRAS on the cell membrane.

Based on the available SHANK3 structural data (SHANK3 SPN-ARR[34,35]) and our recent identification of the conformational opening of the SHANK3 SPN-ARR interface[37], we generated atomistic in silico models of the SHANK3 SPN and SPN-ARR fragments and simulated their binding to the plasma membrane (Supplementary Fig. 3b–e). These simulations indicated that SHANK3 SPN and ARR domains contain positively charged regions that interact with the negatively charged plasma membrane. A recently published NMR structure defined a possible configuration of active KRAS binding to its downstream effector RAF on a lipid nanodisc membrane[43]. Intrigued by the striking structural homology of the RAF RBD (Ras-binding domain) and SHANK3 SPN domains[34,35,43], and our simulation data indicating a SHANK3 SPN-ARR membrane interaction, we generated a simulation model of the SHANK3 SPN-ARR–KRAS complex on the cell membrane (Fig. 3b). We observed that KRAS-bound SHANK3 (SPN-ARR domains) has evident interactions with the plasma membrane in its open configuration (Supplementary Fig. 3b–e[37]). An alignment between the SHANK3 SPN-ARR–KRAS model in an open conformation (Fig. 3b) and the nanodisc-bound KRAS-RAF[43] indicates a strong overlap of SPN with the space occupied by the KRAS-interacting RAF (Fig. 3c and Supplementary Fig. 3b–e). These structural data give mechanistic insight into, and support the notion that, SHANK3 (SPN-ARR) competes with RAF for KRAS binding on the plasma membrane, thus limiting KRAS downstream signalling.

To test this model, we first performed competition assays in vitro. Purified recombinant RAF-RBD and mutant KRASG12V proteins were incubated with increasing His-SHANK3 SPN protein concentrations followed by RAF-RBD pulldown (Fig. 3d). We observed a reduction in KRAS binding to the RAF-RBD beads with increasing concentrations of His-SPN (note that His-SPN and SPN-interacting KRAS are washed away in the pulldown; Fig. 3d). ITC measurements for the interaction between active KRASQ61H and RAF-RBD (Supplementary Fig. 3f; Kd = 1.1 μM ± 0.7 μM) and SHANK3 SPN-ARR (Fig. 2c; Kd = 5.4 μM ± 0.7 μM) under the same buffer conditions showed a relatively small difference in affinities, further strengthening our hypothesis that SHANK3 competes with RAF-RBD for KRAS binding.

We then examined whether KRAS effector recruitment was affected in the absence of SHANK3. Silencing of endogenous *SHANK3* enhanced RAF-RBD and KRASG12V interaction in cells, as determined using an established cell-based FRET assay for KRAS effector recruitment (Fig. 3e)[44]. Collectively, these data indicate that SHANK3 can effectively compete with RAF to interact with mutant KRAS and thus may be able to influence KRAS downstream signalling in cells.

The MAPK/ERK pathway is a critical signalling node in *KRAS*-mutant cancers. Active RAS mutants recruit RAF to signal through this pathway to induce ERK phosphorylation and nuclear translocation, and to promote ERK-dependent cell proliferation[8,9]. We thus sought to test whether the ability of SHANK3 to compete with RAF for active KRAS binding could subsequently modulate downstream MAPK/ERK signalling. Transient overexpression of SHANK3 SPN WT in *KRAS*-mutant HCT-116 cells significantly decreased ERK1/2 phosphorylation (Fig. 3f) and diminished ERK1/2 nuclear translocation in *KRAS*-mutant MIA Paca-2 cells (Fig. 3g). The KRAS-binding-deficient SPN mutant (R12E/K22D), in contrast, did not suppress ERK1/2 phosphorylation (Fig. 3f) or affect ERK1/2 translocation to the nucleus (Fig. 3g). In line with SHANK3 SPN-mediated attenuation of ERK-activity, SHANK3 SPN

https://doi.org/10.1038/s41467-024-52326-1

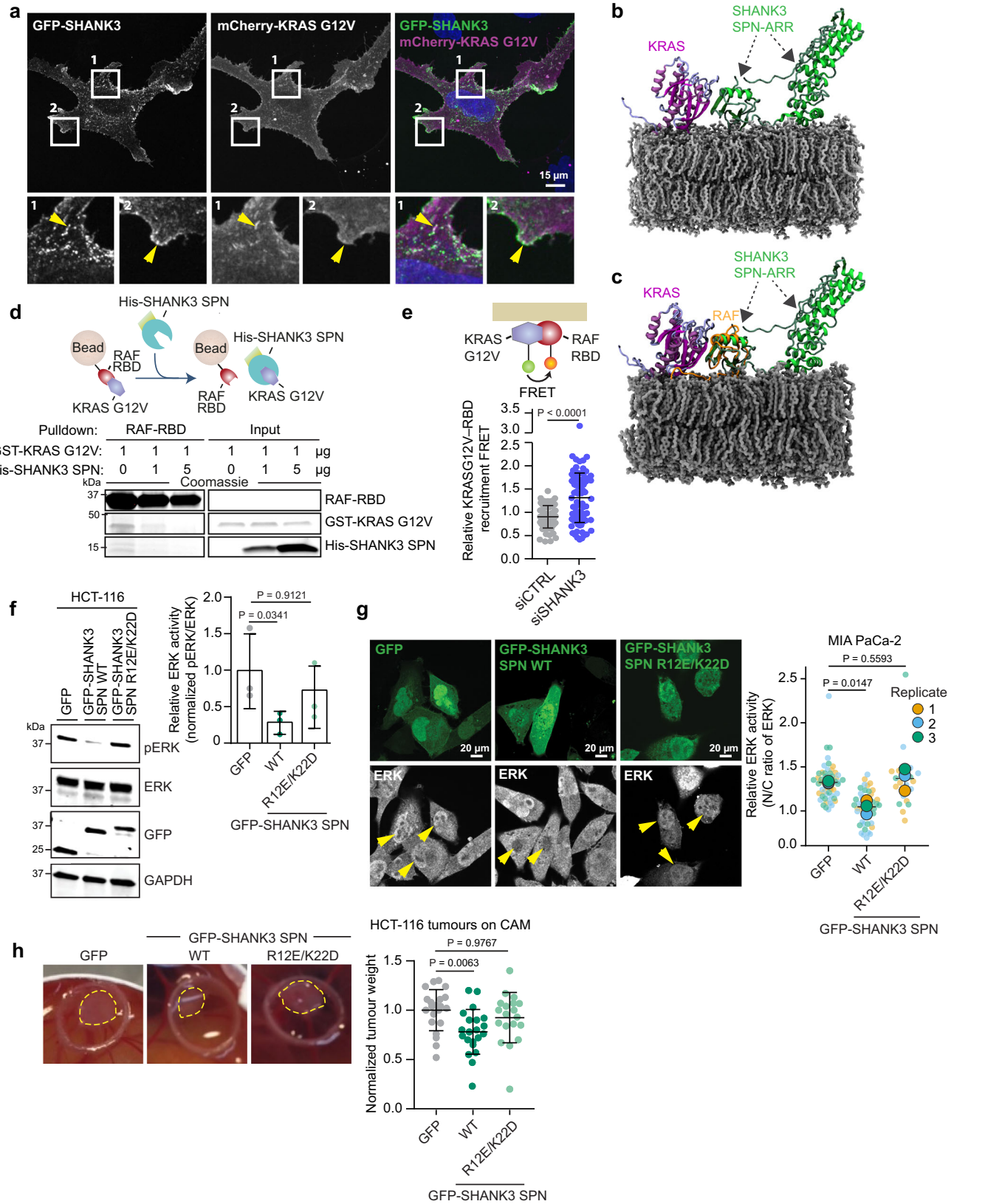


WT overexpression, but not SPN R12E/K22D, in HCT-116 cells restrained *KRAS*-driven tumour growth in the chick embryo CAM CRC xenografts (Fig. 3h).

Together, these data demonstrate that SHANK3 SPN competes with RAF for active KRAS binding and limits oncogenic signalling via the MAPK/ERK pathway.

### *SHANK3* depletion triggers cell death through RAS-MAPK pathway hyperactivation

Recent studies indicate that the level of MAPK/ERK activity in tumour cells needs to be carefully maintained within a precise range; the signalling has to be sufficiently high to support tumour growth and yet below the toxic level that triggers apoptosis or senescence[31–33,45–47].

**Fig. 3 | SHANK3 competes with RAF for the binding of active KRAS and limits downstream MAPK/ERK signalling. a** Representative images of GFP-SHANK3 and mCherry-KRASG12V localisation in A549 cells (maximum projections shown; one experiment with this cell line). Insets and yellow arrows indicate colocalization of GFP-SHANK3 with mCherry-KRASG12V at membrane protrusions. **b** KRAS–SHANK3 SPN-ARR in an open conformation modelled by aligning the RBD and SPN domains of RAF and SHANK3, respectively, on a membrane composed of POPC (1-Palmitoyl-2-oleoyl-sn-glycero-3-phosphocholine)/ Phosphatidylinositol 4,5-bisphosphate/ Cholesterol. **c** Structural alignment between KRAS–SHANK3 SPN-ARR (model) and nanodisc-bound KRAS–RAF complex (PDB:6PTW). **d** Analysis of RAF-RBD–KRAS binding in the presence of the SHANK3 SPN domain using the depicted pulldown assay. Samples were resolved on SDS-PAGE gel and stained with Coomassie. A representative gel is shown (three independent experiments). **e** Quantification of relative FRET efficiency between GFP-KRASG12V (FRET donor) and mRFP-RAF-RBD (FRET acceptor) in siCTRL or siSHANK3 (smartpool SHANK3 siRNA) HEK293 cells. Shown are the individual data points [mean ± s.d., $n = 79$ (siCTRL) or 87 (siSHANK3) from three independent experiments. Unpaired two-tailed Student's $t$-test with Welch's correction]. **f** A representative immunoblot and quantification of ERK activation levels (phospho-ERK1/2 (Thr202/Y204) / total ERK relative to loading) in HCT-116 cells expressing GFP-SHANK3 SPN WT or GFP-SHANK3 SPN R12E/K22D (data represent the individual values; mean ± s.d.; mean of control is set to 1.0 by definition; three independent experiments; Kruskal-Wallis one-way ANOVA and Dunn's post hoc test). **g** Representative confocal images (middle plane) and quantification of nuclear ERK (indicating ERK activity) in MIA PaCa-2 cells. Yellow arrowheads point to representative nuclei. N/C, nuclear to cytoplasmic ratio. Shown are the individual data points and the population average of each biological replicate (mean ± s.d.; three independent experiments; one-way ANOVA with Holm-Sidak's multiple comparison test). **h** Representative images and quantification of tumour growth of HCT-116 cells, transiently expressing GFP-SHANK3 SPN WT or GFP-SHANK3 SPN R12E/K22D, on CAMs. Tumours are delimited by the yellow circles [mean ± s.d.; $n = 21$ (GFP, SPN WT) or 19 (SPN R12E/K22D) tumours from two independent experiments; Kruskal-Wallis one-way ANOVA and Dunn's post hoc test]. Source data are provided as a Source Data file.

We observed a marked increase in ERK1/2 phosphorylation in *SHANK3*-silenced *KRAS*-mutant pancreatic (PANC-1) and lung (A549) cancer cells (Fig. 4a), while AKT activity was not significantly changed (Supplementary Fig. 4a). In some experiments ERK and AKT total protein levels were also decreased upon *SHANK3*-silencing. However, this varied greatly between experiments and was not significant. In contrast, ERK activity was not significantly affected in WT *KRAS* pancreatic (BxPC3) and colorectal (HT-29) cancer cells upon *SHANK3* loss (Supplementary Fig. 4b, c). To further validate these results in living *SHANK3*-silenced cells on the single cell level, we used an ERK kinase translocation reporter (ERK-KTR)[48] that shuttles between the cytoplasm and the nucleus in response to changes in ERK activation state (Fig. 4b). *SHANK3* silencing in PANC-1 cells significantly increased the cytoplasmic-to-nuclear (C/N) ratio of the KTR, indicative of increased ERK activity, compared to control cells. These data further demonstrate that the loss of SHANK3 induces MAPK/ERK signalling hyperactivation in *KRAS*-mutant cells (Fig. 4b).

In addition to ERK hyperactivation, *SHANK3* silencing significantly increased the levels of cleaved-PARP1 in PANC-1 and A549 cells (Fig. 4a, c), and the number of Annexin V/PI-positive PANC-1 cells (Fig. 4d and Supplementary Fig. 5). In contrast, cleaved-PARP1 levels were not markedly increased in WT *KRAS* HT-29 cells in the same conditions (Supplementary Fig. 4c). Moving from 2D to 3D and in vivo, *SHANK3* silencing impaired PANC-1 spheroid formation and growth in Matrigel (Fig. 1b) and significantly increased the number of Annexin V-positive apoptotic cells over time (Fig. 4e). We also detected notably higher cleaved caspase-3 staining in *SHANK3*-silenced *KRAS*-mutant A549 CAM tumours, compared to control tumours (Fig. 4f). These data indicate that loss of SHANK3 induces apoptosis in *KRAS*-mutant cells.

We then asked whether the cytotoxic effects of *SHANK3* silencing in *KRAS*-mutant cells depend on the increased activity of the MAPK/ERK pathway. First, we treated PANC-1 cells with low doses of the MEK inhibitor trametinib and analysed cell proliferation (measured as confluence %) (Fig. 4g–i). In control silenced cells, trametinib inhibited ERK activation (Fig. 4g), but had no effect on cell proliferation (Fig. 4h). In *SHANK3*-silenced cells, trametinib clearly dampened the elevation in ERK activity observed following SHANK3 loss and counteracted the proliferation defect in a dose- and time-dependent manner (Fig. 4g–i, Supplementary Fig. 6a). Of note, we found that the highest trametinib concentration (1 μM) increased SHANK3 protein expression/stability in control cells (Fig. 4g), which is in line with a previous study reporting ERK-mediated downregulation of SHANK3 protein stability in neurons[49]. Next, we measured the proliferation/viability of PANC-1 cells treated with the MEK inhibitor selumetinib or the ERK inhibitor SCH772984. MEK or ERK inhibition had no/modest effect on cell viability of control-silenced cells (Fig. 4j, k; as previously described[50]), whereas both selumetinib and SCH772984 partially rescued the proliferation defect of *SHANK3*-silenced cells in a dose-dependent manner (Fig. 4j, k). Notably, inhibition of integrin signalling with Rap1 or focal adhesion kinase (FAK) inhibitors did not rescue the observed phenotype (Supplementary Fig. 6a–c); However, we cannot formally exclude that Rap1 or FAK functions not influenced by the inhibitors contribute to siSHANK3-induced apoptosis. On the other hand, *KRAS* silencing inhibited *SHANK3*-silencing-induced ERK activation and PARP1 cleavage and showed a modest trend towards increasing cell viability (Supplementary Fig. 6d–f). Finally, we tested whether overexpression of mutant active KRAS would override the inhibition of endogenous SHANK3 and trigger hyperactivation of ERK and apoptosis in *KRAS*-mutant cells. Overexpression of GFP-KRASG12V failed to hyperactivate ERK or trigger substantial apoptosis in A549 cells (Supplementary Fig. 6g, h). This is most likely due to significant upregulation of endogenous SHANK3 (Supplementary Fig. 6g, h), suggesting that *KRAS*-mutant cells are able to fine-tune KRAS signalling via altered SHANK3 expression. The exact mechanism of this crosstalk will be interesting to explore in the future.

These results indicate that the anti-proliferative effects and reduced cell viability triggered by SHANK3 depletion in *KRAS*-mutant cells are linked to dysregulated MAPK/ERK activity and not due to increased integrin signalling in these cells[34].

### *SHANK3* depletion impairs the growth of established *KRAS*-mutant tumours

To evaluate the requirement of SHANK3 in maintaining the growth of established tumours, we generated PANC-1 cell clones with a doxycycline (dox)-inducible shRNA against *SHANK3* (Fig. 5a). Dox-induced *SHANK3* depletion suppressed cell proliferation in vitro similar to the siRNA approach (Fig. 5a–e and Supplementary Figs. 7 and 8). Consistent with the results obtained by siRNA-mediated silencing, inducible silencing of *SHANK3* (shRNA targeting sequence is distinct from the two siRNAs) strongly increased ERK phosphorylation and, consequently, PARP1 cleavage in a time-dependent fashion (Fig. 5b and Supplementary Fig. 7). The induction of *SHANK3* silencing also abolished the growth of established 3D spheroids and was accompanied by a significant increase in AnnexinV-positive regions within the spheroids over time (Fig. 5c–e and Supplementary Fig. 8). To further investigate the apoptotic pathways activated by SHANK3 loss, we analysed the activity of caspases. *SHANK3*-silenced cells showed notably higher caspase-3 and caspase-8 activity in a time-dependent manner (Fig. 5f, g; activity peak at 5 days post dox induction), whereas caspase-9 showed no elevated activity (Supplementary Fig. 9). These data indicate that *SHANK3* depletion induces caspase-3/caspase-8-dependent apoptosis in *KRAS*-mutant cells.

To study the effect of dox-induced *SHANK3* depletion in established tumours in vivo, we implanted sh*SHANK3*-expressing

https://doi.org/10.1038/s41467-024-52326-1

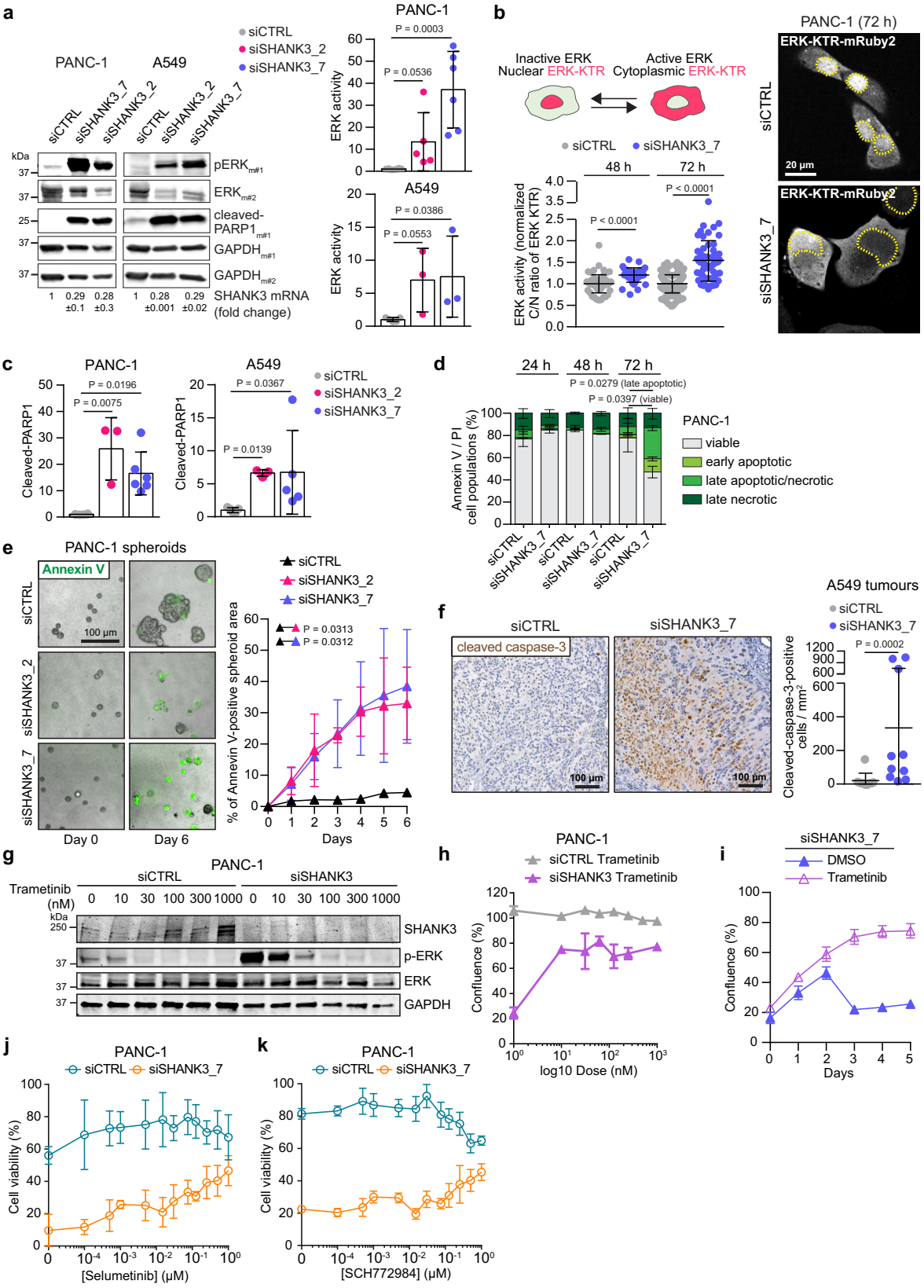


PANC-1 cells into the flanks of athymic Nude mice, allowed tumours to form (~100 mm$^3$) and thereafter subjected the mice to a dox-supplemented or normal diet (Fig. 5h). shRNA induction was monitored by imaging red fluorescence (tRFP reporter) and tumour growth was followed bi-weekly. *SHANK3* depletion in the established tumours led to robust inhibition of tumour growth when compared to control tumours (Fig. 5i, j and Supplementary Fig. 10). At the end of the experiment, *SHANK3* mRNA expression remained significantly suppressed in the dox-induced tumours (Fig. 5k). The reduced growth of established tumours upon *SHANK3*-depletion was also reflected in the tumour masses at the end of the experiment (Fig. 5l). These in vivo data highlight the potential of SHANK3

**Fig. 4 | *SHANK3* depletion triggers RAS-MAPK pathway hyperactivation and apoptosis in *KRAS*-mutant cells. a** ERK activity in PANC-1 and A549 cells post *SHANK3* silencing (3 days). Samples blotted on duplicate membranes, m#1 and m#2. *SHANK3* mRNA levels (fold change) indicated below [mean ± s.d.; PANC-1, $n = 8$ (siCTRL), 5 (siSHANK3_2) or 6 (siSHANK3_7); A549, $n = 5$ (siCTRL) or 3 (siSHANK3_2 and siSHANK3_7) independent experiments; Kruskal-Wallis one-way ANOVA and Dunn's post hoc tests]. **b** Confocal images of ERK-KTR-mRuby2-expressing siCTRL and siSHANK3 cells (nuclei outlined by yellow dashed lines). C/N, ERK-KTR-mRuby2 cytoplasmic/nuclear ratio [mean ± s.d.; $n = 61$ (siCTRL, 48 h), 38 (siSHANK3_7, 48 h), 185 (siCTRL, 72 h) or 59 (siSHANK3_7, 72 h) cells from three independent experiments; unpaired two-tailed Student's *t*-test with Welch's correction]. **c** Immunoblotting analysis of cleaved-PARP1 from 4a [mean ± s.d., normalized to siCTRL; PANC-1, $n = 6$ (siCTRL, siSHANK3_7) or 3 (siSHANK3_2); A549, $n = 5$ (siCTRL, siSHANK3_7) or 3 (siSHANK3_2) independent experiments; Kruskal-Wallis and Dunn's post hoc tests]. **d**, **e** siSHANK3 PANC-1 cell death in 2D (annexin V-FITC flow cytometry analysis, **d**) and 3D (annexin-positive spheroid area, **e**) [mean ± s.d.; five independent experiments; unpaired two-tailed Student's *t*-test with Welch's correction (**d**); one-way ANOVA with Holm-Sidak's multiple comparison test at endpoint (**e**)]. **f** Cleaved caspase-3-postive cells in siSHANK3 A549 tumours (CAM assay) (mean ± s.d.; $n = 10$ tumours from two independent experiments; two-tailed Mann–Whitney test; no/residual siSHANK3 PANC-1 tumours detected). **g** ERK activity in siSHANK3 PANC-1 cells ± MEK inhibitor (trametinib) (two independent experiments). **h** siSHANK3 PANC-1 cell proliferation (confluence % at day 5) ± trametinib (mean ± s.d; $n = 4$ technical replicates; representative of three independent experiments). **i** siSHANK3 PANC-1 cell proliferation ± 300 nM trametinib over time (mean ± s.e.m.; $n = 4$ technical replicates; representative of three independent experiments). **j**, **k** siSHANK3 PANC-1 cell viability ± selumetinib (MEK inhibitor) (**j**) or SCH772984 (ERK inhibitor) (**k**) [mean ± s.d; $n = 4$ (**j**, **k** siSHANK3) or 3 (**k**, siCTRL) technical replicates; representative of three independent experiments]. Source data are provided as a Source Data file.

targeting as an anti-cancer therapy in pre-existing *KRAS*-mutant tumours.

### Nanobodies disrupting the SHANK3-KRAS interaction drive *KRAS*-mutant cells into apoptosis

To further explore the possibility of SHANK3 targeting as a therapeutic vulnerability, we generated nanobodies that interfere with the SHANK3–KRAS interaction and assessed their efficacy in *KRAS*-mutant cancer cells. A phage display library screen identified two distinct single-domain antibody fragments (VHH-binders; nanobodies A01 and E01) directed against the SHANK3 SPN domain. Using MST, the affinity of the E01 nanobody for SHANK3 was determined to be 137 ± 6 nM (Supplementary Fig. 11). We detected clear binding of A01 to SHANK3; however, the relatively low affinity precluded precise affinity determination. Both nanobodies robustly inhibited SHANK3–KRAS-GTP interaction in an enzyme-linked immunosorbent assay (ELISA) as well as in in vitro pull-down assays (Fig. 6a, b). When expressed in cells, both anti-SHANK3 SPN nanobodies co-precipitated endogenous SHANK3 (Fig. 6c). In functional viability studies with *KRAS*-mutant pancreatic (PANC-1) and lung (A549 and H441) cancer cells, both nanobodies increased the number of Annexin V-positive apoptotic cells (Fig. 6d, e and Supplementary Fig. 12). Finally, while control cells rapidly formed tumours in the CAM xenograft model, overexpression of A01 and E01 anti-SHANK3 nanobodies significantly reduced the *KRAS*-driven tumour growth (Fig. 6f). These data indicate that disrupting SHANK3 interaction with KRAS results in a similar loss of cell viability and apoptosis induction in *KRAS*-mutant cells as with RNAi-mediated *SHANK3* depletion (Fig. 6g).

Together, these findings support the concept that hyperactivating the RAS-MAPK pathway in *KRAS*-mutant cells by ablating SHANK3 could have a therapeutic impact on *KRAS*-mutant cancers.

## Discussion

Our work identified the SHANK3 scaffold protein as an essential regulator of active and mutant KRAS. SHANK3 directly interacts with KRAS, competes with RAF for KRAS binding on the plasma membrane, and sets downstream MAPK/ERK signalling to an optimal level to sustain proliferative capacity and prevent active ERK levels from reaching a lethal signalling threshold (Fig. 6g). We demonstrate that by disrupting the SHANK3–KRAS interaction, thus removing an endogenous KRAS signalling brake, we can trigger cytotoxic ERK activity that results in reduced cell proliferation, apoptosis induction and impaired tumour growth in *KRAS*-mutant xenograft models. This indicates that *KRAS*-driven cancer cells require intermediate levels of SHANK3–KRAS association to support tumour growth (Fig. 6g).

Targeting SHANK3 to induce RAS-MAPK hyperactivation-induced apoptosis represents an example of the emerging concept of context-specific lethality of oncogenic pathway activation[51,52]. Firstly, we show that SHANK3 binding to oncogenic KRAS does not depend on specific *KRAS*-activating mutations. Therefore, targeting the SHANK3–KRAS interaction could represent a pan-KRAS-mutant compatible strategy for the selective killing of *KRAS*-mutant cancer cells. Secondly, while the current efforts strive to develop KRAS inhibitors[12,15–17,53], we describe a mechanism to hyperactivate KRAS-MAPK signalling to cytotoxic levels by disrupting KRAS interaction with SHANK3. This is in line with the recently emerging concept of pathway overactivation as an exploitable vulnerability in cancer[33,47,51,52].

We provide proof-of-concept evidence of the ability of inhibitors targeting the SHANK3–KRAS interaction to trigger apoptosis and limit the growth of *KRAS*-mutant cancers. Although targeting intracellular proteins by antibodies has been difficult, the use of nanobodies with nanoparticles and cell-penetrating peptides offers new opportunities[54,55]. Furthermore, pharmaceutical development of small molecule inhibitors of protein-protein interactions has recently become possible, as exemplified by the successful generation of BH3-mimetics[56]. Similarly, several siRNA therapeutics have already gained FDA approval[57–59]. Our findings that *KRAS*-mutant tumour growth can be inhibited in in vivo settings either by modulating *SHANK3* expression or by blocking SHANK3–KRAS protein-protein interaction using nanobodies, demonstrate that SHANK3 might represent a therapeutic vulnerability in *KRAS*-mutant cancers.

Many important questions remain to be investigated regarding the emerging but currently incompletely understood concept of hyperactivation-induced cell death. Focusing here on the SHANK3-dependent pathway, the detailed mechanism of SHANK3 control of ERK signalling is not fully characterized. We show that SHANK3 depletion hyperactivates ERK and induces cell death, which can be rescued by three distinct MEK/ERK inhibitors. However, *KRAS* silencing does not fully restore cell viability and the KRAS-binding SPN-domain alone fails to rescue cell viability in si*SHANK3* cells. These data imply that SHANK3 control of apoptosis extends beyond the KRAS–RAF interaction. SHANK3 is a large multi-domain scaffold protein binding to cell surface receptors and actin in the postsynaptic density of neurons[36,60]. At present, SHANK3 has not been widely investigated beyond the central nervous system and currently unknown protein interactions and biology may enable SHANK3 to control not only ERK activity but its spatial localisation in cells in a manner that contributes to limiting pathway activity. Furthermore, SHANK3 interacts with ERK and ERK regulates SHANK3 stability[49], implying a possibly complex crosstalk between the two proteins.

Oncogene overactivation-induced loss of cell viability was recently reported for several distinct oncogenic pathways and seems in all cases to be dependent on further activation of an already highly active signalling axis[33,51,52]. How cancer cells recognise favourable versus unfavourable levels of oncogenic signalling is not clear. In terms of SHANK3, this recognition may translate into tight modulation of its

https://doi.org/10.1038/s41467-024-52326-1

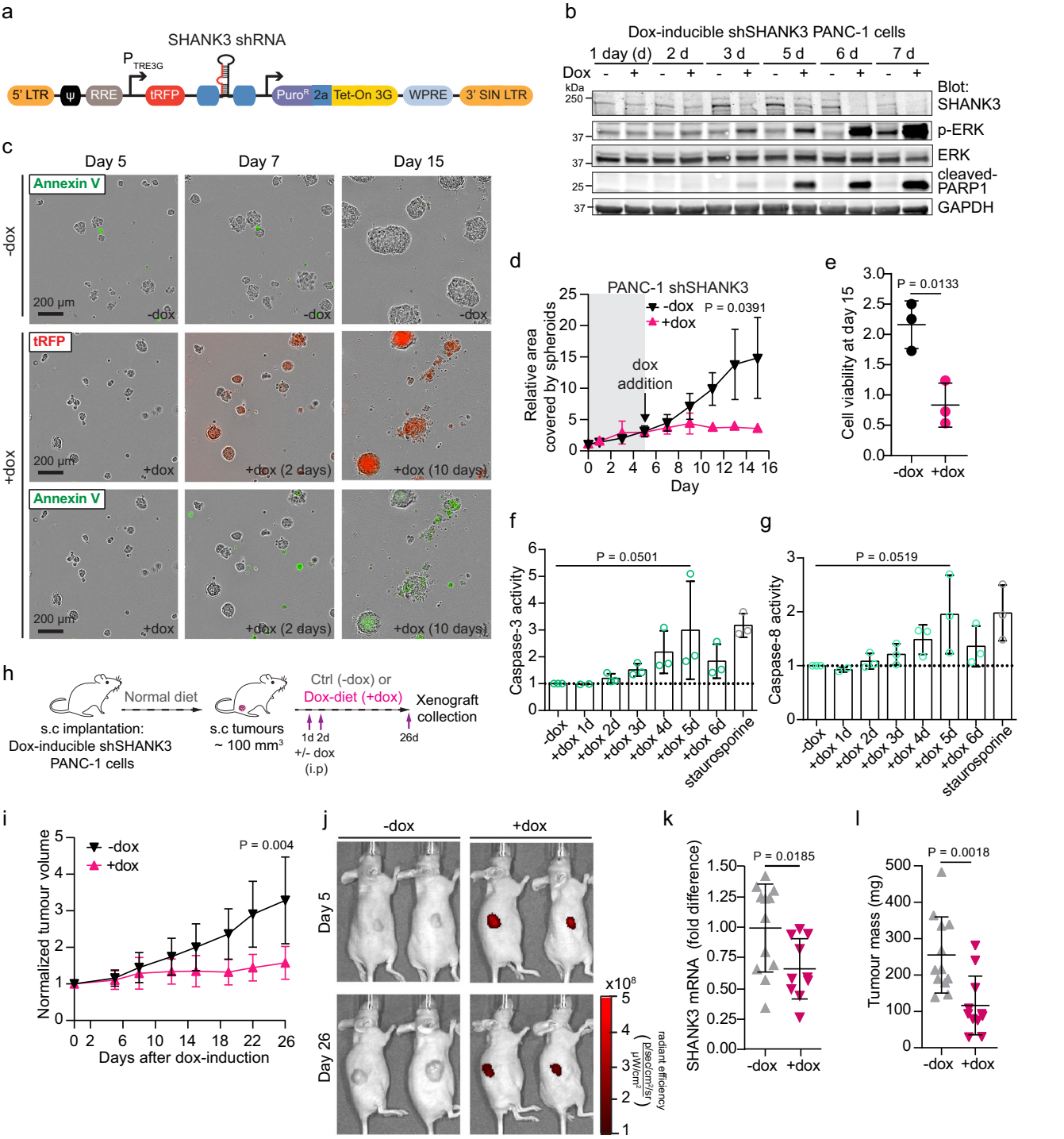


expression levels. We find that overexpression of mutant active KRAS in *KRAS*-mutant cells fails to over-activate KRAS-ERK signalling and trigger cell death, most likely owing to a concomitant upregulation of endogenous SHANK3. Thus, cancer cells seem to optimally regulate oncogenic signalling below a cytotoxic level and we propose SHANK3 inhibition of KRAS interaction as one mechanism employed by *KRAS*-mutant cancer cells to prevent signalling overdose. While the mechanisms regulating SHANK3 expression in cancer remain to be elucidated, investigating the impact of oncogene-induced stress on SHANK3 expression could shed light on its potential involvement in tumorigenesis. In addition, understanding how SHANK3 regulates physiological RAS signalling in response to growth factors or the interplay between SHANK3 and other RAS-binding partners might offer insights into *KRAS*-driven cancer development. Our study has focused on the SHANK3 role in modulating KRAS signalling, however, the SHANK3 RA-like domain can interact with other RAS family members[34,35]. Therefore, it is possible that SHANK3 has a broader role in other RAS-isoform-driven cancers but this remains to be validated. Lastly, while the safety concerns regarding SHANK3 targeting are mitigated by the observation that individuals with genetic *SHANK3* loss (Phelan-McDermid syndrome) do not exhibit increased tumour formation, this aspect requires thorough investigation.

In summary, our work provides an important example of conditional pathway activation limiting viability of *KRAS*-mutant cancers. We have discovered here that SHANK3 control of ERK activity is essential for cancer cell viability. Therefore, SHANK3 emerges as a

**Fig. 5 | *SHANK3* depletion impairs the growth of pre-existing *KRAS*-mutant PDAC tumours. a** A schematic representation of the lentiviral vector for tetracycline/doxycycline (dox)-inducible synthesis of *SHANK3* shRNA with a tRFP (TurboRFP) reporter for visual confirmation of shRNA expression following dox induction. 5′LTR, 5′long terminal repeat; Ψ, Psi packaging sequence; PuroR, puromycin resistance gene; 2a, self-cleaving peptide; WPRE, Woodchuck Hepatitis Post-transcriptional Regulatory Element; 3′ SIN LTR, 3′ Self-inactivating Long Terminal Repeat (see methods for more detail). **b** ERK activation kinetics in sh*SHANK3 KRAS*-mutant cells. Representative immunoblots showing SHANK3, p-ERK and cleaved-PARP1 levels in control (-dox) and dox-induced (+dox) sh*SHANK3*-expressing PANC-1 cells (mix of two independent clones) collected at different time points. GAPDH, loading control ($n$ = three independent experiments). **c**–**e** Analysis of the growth and viability of sh*SHANK3*-expressing PANC-1 spheroids ± dox (dox added at day 5, when spheroids were established, and continued until day 15). Representative images show *SHANK3* depletion as observed by the tRFP reporter and apoptotic Annexin V-positive cells (**c**). Quantification of spheroid growth over time (**d**), shaded region denotes sphere growth prior to treatment and cell viability at endpoint (**e**) (mean ± s.d. from $n = 3$ independent experiments; unpaired two-tailed Student's $t$-test with Welch's correction at endpoint). **f**, **g** Caspase-3 (**f**) and caspase-8 activity (**g**) in sh*SHANK3*-expressing PANC-1 cells ± dox at the indicated time points (shown is normalized fluorescence intensity). Staurosporine used as a positive control (mean ± s.d.; $n = 3$ independent experiments; one-way ANOVA with Holm-Sidak's multiple comparison test)**. h**–**l** Analysis of the growth of established tumours in mice following *SHANK3* depletion. **h** Outline of animal experiments. **i** Tumour volumes after starting the dox treatment (normalised to tumour volumes at the start of dox induction). **j** Representative IVIS images of the tRFP reporter expression in tumours 5 and 26 days after dox induction. **k** *SHANK3* gene expression (mRNA levels) in tumours at the end of the experiment. **l** Tumour weights at the end of the experiment (26 days after dox-induction) (data represent individual tumours and the mean ± s.d.; $n = 11$ (-dox) and 12 (+dox) tumours; unpaired Student's $t$-test with Welch's correction). Source data are provided as a Source Data file.

cancer vulnerability across different *KRAS*-mutant cells and cancer types.

## Methods

All animal experiments were ethically assessed and authorised by the National Animal Experiment Board and in accordance with The Finnish Act on Animal Experimentation (Animal license numbers ESAVI/9339/2016 and ESAVI/37571/2019). All experiments respected the maximum tumour diameter (15 mm) permitted by the authorisation bodies.

### Cell lines and culture

All cell lines were purchased from ATCC, unless otherwise indicated. PANC-1 (Cat. no. CRL-1469), AsPC-1 (Cat. no. CRL-1682) SW1990 (Cat. no. CRL-2172) PaTu8902 (Cat. no. ACC 179, DSMZ), MIA PaCa-2 (Cat. no. CRL-1420) (*human* pancreatic ductal adenocarcinoma cell lines), A549 (*human* lung adenocarcinoma) (Cat. no. CCL-185), HCT-116 (*human* colorectal carcinoma) (Cat. no. CCL-247), HT-29 (*human* colorectal adenocarcinoma) (Cat. no. HTB-38) and HEK293 (*human* embryonic kidney) (Cat. no. CRL-1573) cells were grown in DMEM (Dulbecco's modified Eagle's medium; Cat. no. D5796, Sigma-Aldrich) supplemented with 10% FBS and 2 mM L-glutamine (Cat. no. G7513-100ML, Sigma-Aldrich).

Su86.86 (*human* pancreatic adenocarcinoma) (Cat. no. CRL-1837), YAPC (*human* pancreatic carcinoma) (Cat.no. ACC 382, DSMZ), H441 (*human* lung adenocarcinoma) (Cat. no. HTB-174), HCT-15 (*human* colorectal adenocarcinoma) (Cat. no. CCL-225), H292 (*human* lung carcinoma) (Cat. no. CRL-1848) and H226 (*human* lung squamous cell carcinoma) (Cat. no. CRL-5826) cells were cultured in RPMI-1640 medium supplemented with 10% FBS and 2 mM L-glutamine.

BxPC-3 (Cat. no. CRL-1687) and Panc10.05 (Cat. no. CRL-2547) (*human* pancreatic adenocarcinoma) cells were cultured in RPMI-1640 medium supplemented with 10% FBS and 2 mM L-glutamine plus 10 units/ml *human* recombinant insulin (Cat. no. I9278-5ML, Sigma-Aldrich) for the Panc10.05 cells only. ARPE-19 (*human* retinal pigmented epithelium) (Cat. no. CRL-2302) cells were grown in DMEM:F12 (Cat. no. 11320074, Gibco) supplemented with 10% FBS and 2 mM L-glutamine.

Cells were regularly tested by MycoAlert™ Mycoplasma Detection Kit (Cat. no. LT07-418, Lonza) with MycoAlert™ Assay Control Set (Cat. no. LT07-518, Lonza) and found to be free from mycoplasma contamination. All cell lines were authenticated by STR profiling using the services of the Leibniz Institute DSMZ.

### siRNAs and DNA constructs

The siRNAs used were SMARTpool ON-TARGETplus *Human SHANK3* siRNA (Cat. no. L-024645-00-0010, Dharmacon™, Horizon Discovery), individual *Human SHANK3* siRNA_2 (Cat. no. S100717710 Hs_SHANK3_2 siRNA, Qiagen; target sequence: 5′-CAGGGATGTCC GCAACTACAA -3′), individual ON-TARGETplus *Human SHANK3* siRNA_7 (Cat. no. J-024645-07, Dharmacon™, Horizon Discovery; target sequence: 5′- GGGCTTCACCTGACTACAA -3′) and ON-TARGETplus *Human KRAS* siRNA SMARTpool (Cat. no. L-005069-00-0010, Dharmacon™, Horizon Discovery). The control siRNA was Allstars negative control siRNA (Cat. no. 1027281, Qiagen).

EGFP-tagged SPN domain and mRFP-tagged SHANK3 were generated previously[34]. pHAGE-EGFP-Shank3 (GFP-SHANK3 WT) was kindly supplied by Alex Shcheglovitov. The R12E/K22D mutation was introduced by site-directed mutagenesis (Gene Universal). pmGFP-KRASG12V and mRFP-RBD with the RAS binding domain (RBD) of CRAF have been described earlier[61,62]. The pmCherry-KRASG12V construct was generated by replacing pmGFP from pmGFP-KRASG12V with pmCherry from the pmCherry-C1 vector (Clontech Laboratories Inc.) using NheI and BsrGI restriction sites. DsRed-KRASG12V has been described before[63] and was a gift from James Lorens. His6-KRASQ61H (Plasmid #25153, Addgene) was a gift from Cheryl Arrowsmith. pLentiPGK-Blast-DEST-ERKKTRmRuby2 (Plasmid #90231, Addgene) was a kind gift from Markus Cover[48]. mCherry-tagged anti-SHANK3-SPN nanobodies A01 and E01 were generated by Hybrigenics. In addition, peGFP-C1 and pHAGE-CMV-eGFP-W (PlasmID, Harvard Medical School) and pmCherry-C1 were used as controls.

### Generation of ERK biosensor cells

HEK293T packaging cells were co-transfected with pMDLg/pRRE (Plasmid #12251, Addgene), pRSV-Rev (Plasmid #12253, Addgene), pMD2.G (Plasmid #12259, Addgene) and pLentiPGK-Blast-DEST-ERKKTRmRuby2, using Lipofectamine 3000 (Cat. no. L3000-015, Life Technologies) as per the manufacturer's instructions. Packaged lentiviruses were then applied to PANC-1 cells in the presence of polybrene (8 μg/ml, Cat. no. TR-1003-G, Sigma-Aldrich) and incubated overnight. Successfully transduced cells were then selected using blasticidin (6 μg/ml, Cat. no. 15205, Sigma-Aldrich).

### Generation of doxycycline-inducible sh*SHANK3* PANC-1 cell line

SMART lentiviral shRNA vectors for doxycycline-inducible suppression of human *SHANK3* gene expression were purchased from Dharmacon as viral particles (Dox-inducible SMARTvector sh*SHANK3*, Cat. no. V3SH7669-228381856, Dharmacon). The lentiviral vector contains a PTRE3G inducible promoter (Fig. 5a). The tetracycline response element is activated by the Tet-On® 3 G transactivator protein in the presence of dox. The vector also contains a TurboRFP reporter (visual tracking of expression upon dox induction), a puromycin resistance gene, a self-cleaving peptide (enables the expression of both PuroR and Tet-On® 3 G transactivator from a single RNA pol II promoter) and Tet-On® 3G (encodes the dox-regulated transactivator protein, which binds to PTRE3G promoter in the presence of dox).

https://doi.org/10.1038/s41467-024-52326-1

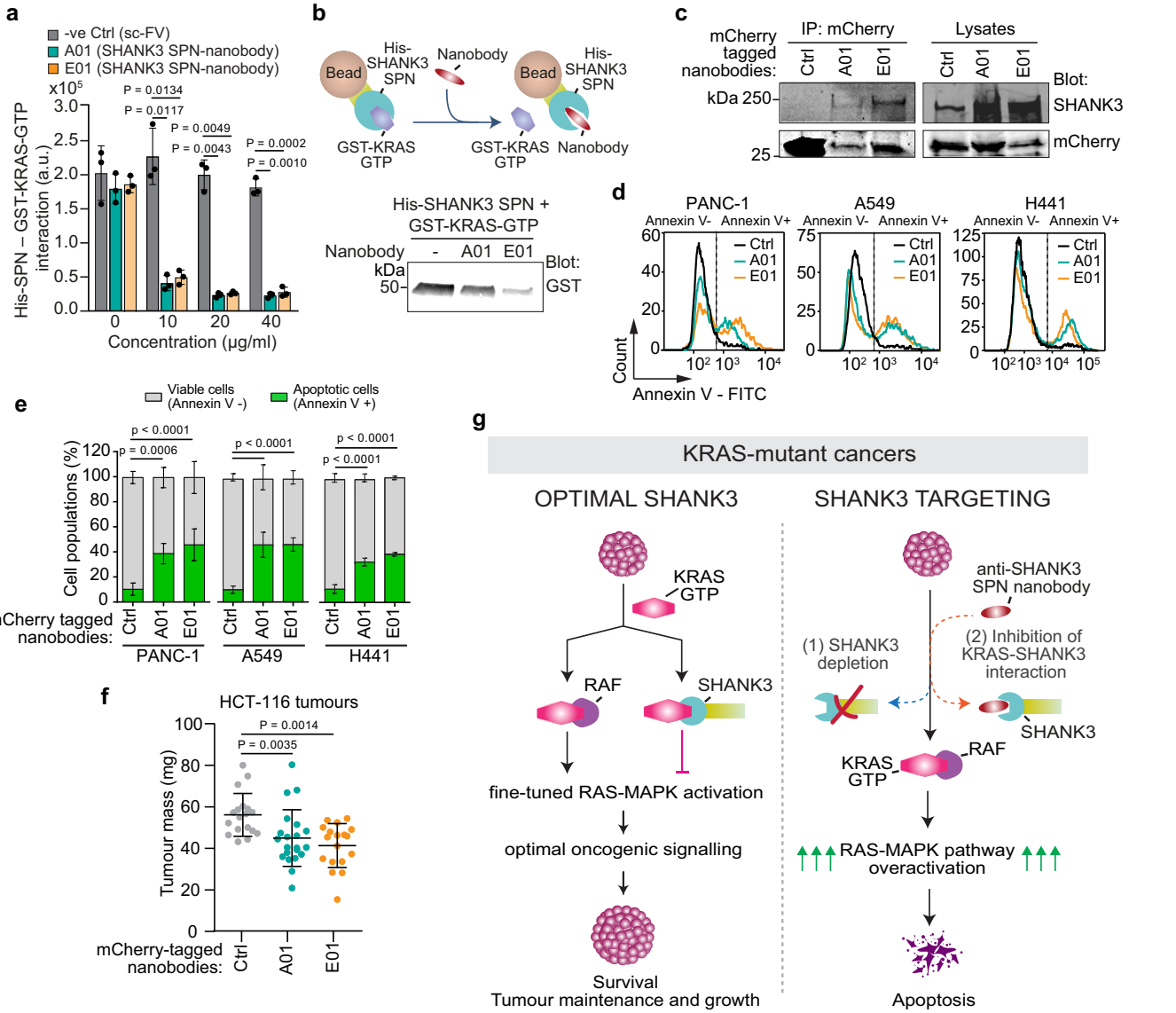


**Fig. 6 | Targeting of KRAS–SHANK3 interaction by anti-SHANK3 nanobodies induces apoptosis and inhibits *KRAS*-driven tumour growth. a–c** The inhibitory function of anti-SHANK3 SPN nanobodies on KRAS–SHANK3 interaction. **a** The effect of two independent SHANK3 SPN nanobodies (A01 and E01) at the indicated concentration on the binding of His-tagged SHANK3 SPN to GST-tagged KRAS-GTP as measured by ELISA (data are mean ± s.d. of the Eu-signal; three independent experiments; Unpaired two-tailed Student's *t*-test with Welch's correction). **b** Top: The experimental outline showing His-SHANK3 SPN pulldown of GST-KRAS-GTP in the presence of anti-SHANK3 SPN nanobodies. Bottom: A representative blot showing loss of SHANK3–KRAS interaction in the presence of the nanobodies ($n = 2$ independent experiments). **c** Specificity analysis of anti-SHANK3 SPN nanobodies. A549 cells expressing mCherry alone (control; Ctrl) or mCherry-tagged anti-SHANK3 SPN nanobodies (A01, E01) were subjected to IP. A representative western blot, probed with the indicated antibodies is shown ($n = 2$ independent experiments). **d**, **e**, Analysis of cell viability in the presence of anti-SHANK3 nanobodies. Representative flow cytometry assay histograms (**d**) and quantification (**e**) of apoptosis (Annexin V-FITC-positive (+) cells) in PANC-1, A549 and H441 cells, expressing mCherry (Ctrl) or mCherry-tagged anti-SHANK3 SPN-nanobodies, 4 days after transfections [mean ± s.d.; $n = 3$ (PANC-1) and 4 (A549) independent experiments; two-way ANOVA and Sidak's post hoc test; example scatter plots and gating strategy are shown in Supplementary Fig. 12]. **f** Analysis of tumour growth with HCT-116 cells transiently expressing mCherry-tagged anti-SHANK3 SPN nanobodies (A01 and E01) or mCherry (Ctrl) and inoculated on CAM membranes (data represent individual tumours and the mean ± s.d.; $n = 18$ (Ctrl, E01) or 21 (A01) tumours/treatment group; Kruskal-Wallis one-way ANOVA and Dunn's post hoc test). **g** Schematic model of SHANK3-controlled cell fate in *KRAS*-mutant cancers. SHANK3 directly interacts with active KRAS and competes with RAF for KRAS binding to sustain oncogenic RAS-MAPK/ERK signalling at an optimal level (i.e. below toxic oncogenic signalling) in *KRAS*-mutant cancers. SHANK3 loss (1) or inhibition of SHANK3–KRAS interaction (2) drive *KRAS*-mutant cells into cell death. Source data are provided as a Source Data file.

Packaged lentiviruses (40 MOI) were applied to PANC-1 cells in the presence of polybrene (8 µg/ml) for 48 h; first, cells were incubated with the transduction mix in serum-free medium for 20 h, and then full medium was added to cells without removing the transduction mix. Two days after transduction, the medium was replaced with full medium and cells were cultured for an additional 48 h. Four days after transduction, cells were selected using puromycin (4 µg/ml, Cat. no. 15205, Sigma-Aldrich). Single-cell clones were created by screening for high induction efficacy (bright tRFP-positive clones after dox-induction, indicative of shRNA expression). All established PANC-1 sh*SHANK3* expressing cell lines (single and a mix of clones 1C and 4S) were cultured in DMEM supplemented with 10% FBS and 2 mM L-glutamine, 2 µg/ml puromycin. For doxycycline inductions, treatment (+dox; 1–2 µg/ml) was

started 24 h post-plating. Culture medium (+/- dox) was changed every 2nd day.

### Transient transfections

Lipofectamine 3000 and P3000™ Enhancer Reagent (Cat. no. L3000001, Thermo Fisher Scientific) or jetPRIME (Cat. no. 101000046, Polyplus) were used to transiently transfect cells with plasmids according to the manufacturer's protocol. siRNA silencing was performed using 30–67 nM siRNA (siRNA targeting *SHANK3* or negative control siRNA) and Lipofectamine® RNAiMAX Reagent (Cat. no. 13778075, Thermo Fisher Scientific) according to the manufacturer's protocol. Cells were cultured for 24 h with transfection reagents and, one day post-transfection, medium was changed to full culture medium, and cells were used for the experiments at the indicated time points.

### Proliferation assays using IncuCyte

2D assay: Cells were seeded on a 96-well plate and transfected with siRNAs on the following day, as described above. To perform a proliferation screen in multiple cancer cell lines, 5000–10000 cells were seeded in the 96-wells depending on the growth rate of control cells.

Inhibitor treatments were started a day post-silencing and cells were treated with complete medium containing DMSO (control), Trametinib (Cat. no. GSK1120212, Selleckchem), Rap1 inhibitor (Cat. no. GGTI 298, Sigma) or FAK inhibitor (FAK-14, Sigma) at the indicated concentrations. For sh*SHANK3* PANC-1 cells, dox induction (+dox; 2 μg/ml) was started 24 h post-plating. Culture medium with or without dox was changed every other day. Proliferation was measured for 4 days.

3D spheroid assay: Spheroid formation was performed with cells embedded between two layers of Matrigel[64]. Briefly, the inner wells of an angiogenesis 96-well μ-plate (Cat. no. 89646, Ibidi GmbH) were coated with 10 μl of 50% Matrigel (diluted in full cell culture medium; Matrigel stock 9 mg/ml, Cat. no. 354230, Corning), centrifuged for 20 min at 200 g (4 °C) and incubated for 1 h at 37 °C. Next, the upper wells were filled with 20 μl of cell suspension in 25% Matrigel (500 cells/well), centrifuged for 10 min at 100 x g and incubated at 37 °C for 4–16 h. Wells were then filled with complete culture medium and spheroid formation was measured for 6–15 days. SHANK3 depletion was induced by doxycycline ( + dox; 2 μg/ml) in established sh*SHANK3* PANC-1 spheroids at day 5. Annexin V (1:200, Annexin V-FITC Apoptosis Detection Kit, Cat. no. BMS500FI-300, eBioscience™) was added at the same time as dox and spheroid growth and apoptosis were monitored for 10 days. Culture medium (+/- dox and Annexin V) was changed every other day.

For both 2D and 3D assays, proliferation was measured using the IncuCyte S3 Live-Cell Analysis system (10x objective). Wells were imaged every 2 h (brightfield). Culture medium was changed every 2–3 days. Analysis was performed using IncuCyte S3 software. The analysis definition was set using the following parameters: segmentation (background-cells), clean-up (hole fill), filters (area, eccentricity, mean intensity, integrated intensity). A mask was set to the best fit of cell confluence to quantify the area covered by cells. Normalised proliferation was calculated from time-lapse imaging by dividing the area covered by cells at every time point by the area of the first time point ($t = 0$; averaged reading used from replicate wells).

### Colony formation

Cells previously silenced with the indicated siRNAs for 24 h were seeded on a 6-well plate (250 cells/well) in full medium. The culture medium was changed every 2–3 days, ending the assay on day 10–14. Colonies were fixed with 4% paraformaldehyde (PFA) in phosphate-buffered saline (PBS) for 15 min and washed with PBS. Then, colonies were stained with 0.2% crystal violet in 10% ethanol for 10 min at room temperature and washed with PBS. Plates were scanned and analysed using a Colony area ImageJ plugin[65].

### Cell viability assays

Annexin V-FITC/PI flow cytometry was used to evaluate apoptotic and necrotic cell death in cells cultured in monolayers. One to three days after silencing or four days post transfection of mCherry-tagged anti-SHANK3 nanobodies (A01 and E01) or control-mCherry, cells were stained by Annexin V-FITC Apoptosis Detection Kit (Cat. no. BMS500FI-100, eBioscience™) according to the manufacturer's instructions. Apoptotic cells were detected using BD LSR Fortessa™ analyser (BD Biosciences).

The viability of *SHANK3*-silenced PANC-1 cells treated with ERK and MEK inhibitors was measured using Cell Counting Kit-8 (WST-8/CCK-8; Cat. no. ab228554, Abcam). Cells were silenced for 24 h as described above and then seeded on a 96-well plate with full medium containing DMSO (control), Selumetinib (ADZ6244; Cat. no. S1008, Selleckchem) or a selective ERK1/2 inhibitor (SCH772984; Cat. no. S7101, Selleckchem) at different concentrations (concentrations used: 0, 0.1 nM, 0.5 nM, 1 nM, 5 nM, 10 nM, 31.3 nM, 62.5 nM, 124 nM. 250 nM, 500 nM and 1 μM). Cell viability was measured 96 h after silencing (drugs for 72 h). For some 3D spheroid assays, growth/viability was measured using Cell Counting Kit-8 (WST-8/CCK-8; Cat. no. ab228554, Abcam) instead of IncuCyte. At culture end point, the medium was replaced with fresh medium supplemented with WST-8 solution and, after a 2 h incubation in the dark at 37 °C, absorbance was measured at 460 nm.

### Caspase activity assay

PANC-1 cells expressing doxycycline-inducible *SHANK3* shRNA were seeded in a 96-well plate (4000 cells/well) and treated with doxycycline (2 μg/ml) for 1–6 days. Untreated cells and cells treated for 24 h with staurosporine (2 μM) were used as controls. The activity of caspase-3, caspase-8 and caspase-9 was measured using a commercial kit (Cat. no. ab219915, Abcam) according to the manufacturer's instructions. Briefly, each caspase substrate as a 1X solution was diluted in 100 μl assay buffer per well and added to cells. Cells were incubated at room temperature in the dark for 30–60 min and caspase activity was evaluated by measuring fluorescence intensity (Ex/Em = 535/620 nm [red] for caspase-3, Ex/Em = 490/525 [green] for caspase-8 and Ex/Em = 370/450 nm [blue] for caspase-9) with a Synergy H1 Hybrid Multi-Mode reader (BioTek, Winooski, VT).

### Quantitative real-time polymerase chain reaction (qRT-PCR)

Total cellular RNA was extracted using the NucleoSpin® RNA kit (Cat. no. 740955.50 Macherey-Nagel), and 1 μg of the extracted RNA was used as a template for cDNA synthesis by high-capacity cDNA reverse transcription kit (Cat. no. 4368814, Applied Biosystems) according to the manufacturer's protocol. Tumours were homogenised with T 25 ULTRA-TURRAX® (Ika), and total RNA was extracted using TRIsure™ (Cat. no. BIO-38032, Bioline Ltd). Expression levels of *SHANK3* were determined by TaqMan® qRT-PCR reaction using QuantStudio™ 12 K Flex Real-Time PCR System (Thermo Fisher Scientific). The level of glyceraldehyde 3-phosphate dehydrogenase (*GAPDH*) expression was used as a reference (endogenous control). Taqman® Universal Master Mix II included the necessary components for qRT-PCR reactions (Cat. no. 4440040, Thermo Fisher Scientific). TaqMan® Gene Expression Assays (Thermo Fisher Scientific) were used to detect *SHANK3* (Assay ID: Hs00873185_m1) and *GAPDH* (Assay ID: Hs02786624_g1). Relative quantification (RQ) of *SHANK3* levels was derived from three technical replicates by a comparative CT (ΔΔCT) method using *GAPDH* levels as a reference. RQ_{min} = 2^{-(ΔΔCt + SE)} and RQ_{max} = 2^{-(ΔΔCt - SE)}, where SE is the standard error of the ΔΔCt values.

### Immunoblotting

Inhibitor treatments [DMSO control, Trametinib (GSK1120212, Selleckchem), Rap1 inhibitor (GGTI 298, Sigma) or FAK inhibitor (FAK-14, Sigma)], in complete medium at the indicated

concentrations, were started 1 h before siRNA-mediated silencing and repeated 48 h later.

Cells were collected in lysis buffer [50 mM Tris-HCl (pH 7.5), 150 mM NaCl, 0.5% Triton-X, 0.5% glycerol, 1% SDS, complete protease inhibitor (Sigma-Aldrich) and PhosSTOP (Sigma-Aldrich)] and protein extracts were sonicated. Protein levels were measured using a Bio-Rad protein quantification kit. Sample buffer was added, and samples were boiled for 5 min at 95 °C. Proteins were then separated using SDS-PAGE under denaturing conditions (4–20% Mini-PROTEAN TGX Gels) and transferred onto nitrocellulose membranes by semi-dry turbo blot (BioRad Laboratories). Membranes were blocked with 5% bovine serum albumin (BSA) in TBST (Tris-buffered saline and 0.1% Tween 20) for 1 h at room temperature. Primary antibodies were diluted in 5% BSA in TBST and incubated with membranes overnight at 4 °C. After primary antibody incubation, membranes were washed thrice with TBST for 5 min at room temperature. Fluorophore-conjugated or ECL HRP-linked secondary antibodies (GE Healthcare) were diluted 1:5000 in 5% BSA in TBST or in blocking buffer (Cat. no. 37538, Thermo Fisher Scientific) in PBS (1:1) and were incubated with membranes for 1h at room temperature. Membranes were scanned using an infrared imaging system (Odyssey; LI-COR Biosciences) or using ECL Plus Western blotting reagent (Cat. no. RPN2232, GE Healthcare) and film. Band intensity was determined using Fiji[66] (ImageJ; National Institutes of Health) or Image Studio Lite (LI-COR).

The following primary antibodies were used: SHANK3 (Cat. No. HPA003446, Atlas antibodies and Cat. no. sc-30193, Santa Cruz), GFP (Cat. no. ab1218, Abcam), KRAS (Cat. no. WH0003845M1, Sigma-Aldrich), GAPDH (Cat. no. 5G4-6C5, Hytest), HSP70 (Hsc70/Hsp73; Cat. no. ADI-SPA-815, Enzo), phopho-ERK1/2 (Thr202/Tyr204;Cat. no. 4370S, Cell Signalling), ERK1/2 (Cat. no. 91025, Cell Signalling), phospho-AKT (Ser473) (Cat. no. 9271, Cell Signalling), AKT (Cat. no. 9272, Cell Signalling) and cleaved-PARP1 (Cat. no. ab4830 and ab32064 [E51], both from Abcam; recognise a larger 89 KD and a smaller 28 KD band, respectively). All primary antibodies were used at 1:1000 dilution, except the SHANK3 antibody, which was used at a 1:100 (Cat. no. sc-30193, Santa Cruz) or 1:500 (Cat. No. HPA003446, Atlas antibodies) dilution.

### Co-immunoprecipitations and pulldown assays

HEK293 cells were transiently transfected with (1) mRFP-tagged SHANK3 WT together with GFP-tagged KRASG12V or control (GFP only); or (2) GFP-tagged SHANK3 SPN WT, SHANK3 SPN R12E/K22D or control (GFP only) together with dsRed-tagged KRASG12V. A549 cells were transiently transfected with the control plasmid (pmCherry) or the nanobodies (pmCherry-A01 or pmCherry-E01). 24 h post-transfection the cells were lysed using IP-lysis buffer (40 mM Hepes-NaOH, 75 mM NaCl, 2 mM $MgCl_2$, 1% NP40, protease and phosphatase inhibitors), cleared by centrifugation, and subjected to immunoprecipitation of RFP/mCherry/dsRed-tagged or GFP-tagged fusion proteins using RFP-trap or GFP-trap matrix (Cat. no. rtma-100 and gtma-100, Chromotek), respectively. Input and precipitate samples were analysed by immunoblotting. The KRAS pulldown assays were done by incubating the indicated recombinant proteins with RAF-RBD glutathione affinity beads from the Ras Pull-Down Activation Assay Biochem Kit (Cat. no. BK008, Cytoskeleton) according to the manufacturer's instructions.

### Production and purification of recombinant proteins

All proteins were produced in *E. coli* BL21 cultures using IPTG induction and verified with sodium dodecyl sulphate polyacrylamide gel electrophoresis (SDS-PAGE).

**KRASG12V**. The sequence of the synthetic gene of *KRAS* 4B was designed according to *E.coli* codon usage. *KRAS* was PCR amplified and cloned into a modified pGEX vector (GE Healthcare, Chicago, IL). The G12V mutation to KRAS 4B was purchased from BioCat (https://www1.biocat.com).

Glutathione S-transferase (GST) fusion KRASG12V protein was expressed in Terrific Broth (TB) medium (2.4% w/v yeast extract, 1.2% w/v tryptone, 0.5% w/v glycerol, 0.017 M KH2PO4, 0.072 M K2HPO4, 100 μg/ml Ampicillin) by the addition of 0.4 mM isopropyl-β-D-1-thio-galactopyranoside (IPTG) at 20 °C for 20 h using *E. Coli* BL21 Gold cells. The cells were lysed by sonication on ice (Sonopolus 4000) at 40% amplitude (4x, 1 s pulse on and 1 s pulse off) for 1 min and subsequently centrifuged at 35000 g for 30 min at 4 °C to clear the lysate. The GST KRASG12V fusion protein was purified with Protino Glutathione Agarose 4B (Macherey-Nagel, Düren, Germany) and GST was cleaved by Tobacco Etch Virus (TEV) protease (Invitrogen, Life Technologies, Carlsbad, CA) at 4 °C for 16 h. The TEV protease cleavage extended KRASG12V construct in the N-terminal by four amino acid residues, G, A, M and G. The proteins were further purified by size exclusion chromatography (SEC) with a HiLoad 26/60 Superdex 200 pg column (GE Healthcare, Chicago, IL) in SEC buffer (50 mM Tris, pH 7.3, 300 mM NaCl, 1 mM DTT, 0.1% CHAPS) using an ÄKTA pure chromatography system (GE Healthcare). The protein was concentrated with Amicon ultracentrifugal 10 K filter device (Millipore, Sigma, Burlington, MA). The homodispersity of the proteins was verified with SDS-PAGE.

**KRASQ61H**. The plasmid containing *human* His6-KRASQ61H activating oncogenic mutant (residues 1-169) was a gift from Cheryl Arrowsmith (Plasmid #25153, Addgene). The protein was expressed using *E.coli* BL21(DE3) competent cells (Invitrogen) cultured in Luria Broth (LB) medium. Cells were grown at 37 °C in LB medium supplemented with antibiotics to an OD600 of 0.6, cooled to 18 °C and induced using 300 μM IPTG for 16 h. Cells were pelleted by centrifugation and resuspended in 20 mM $Na_2HPO_4$ pH 7.4, 500 mM NaCl, 5 mM $MgCl_2$, 2 mM DTT and 25 mM imidazole, treated with protease cocktail inhibitor VII (Cat. no. 539138, Calbiochem) and sonicated on ice. The protein was purified using nickel-affinity chromatography with a linear gradient of lysis buffer containing 500 mM imidazole, but without DTT. Immediately after purification, 2 mM DTT was added to the protein fractions. Protein purity was checked by SDS-PAGE. Bound nucleotide was exchanged for GDP or non-hydrolysable GTP analogue GMPPCP using alkaline phosphatase beads (Sigma-Aldrich) and following the protocol of John et.al.[67].

**RBD domain of B-Raf**. The RBD domain of *human* BRAF (Uniprot P15056) corresponding to residues Ser151-Leu232 was cloned into pOPNB vector (OPPF-UK) from codon-optimised synthetic DNA at GeneMill facility, University of Liverpool. The protein was expressed using BL21 competent cells (Invitrogen) cultured in LB and purified using Ni-NTA column with standard protocol. His-tag was cleaved with recombinant His-tagged 3 C protease and removed by a reverse pass on the Ni-NTA column.

**SPN domain of SHANK3**. His-tagged SPN protein was expressed in TB medium with 100 μg/ml ampicillin by the addition of 0.4 mM IPTG at 18 °C for 20 h in *E. coli* BL21 Gold cells. Prior to cell lysis, small amounts of both lysozyme and DNase were added and then the cells were lysed by sonication on ice (Sonopolus 4000) at 40% amplitude (4x, 1 s pulse on and 1 s pulse off) for 1 min and subsequently centrifuged at 15000 g for 60 min at 4 °C to clear the lysate. The His-SPN fusion protein was purified with Protino Ni-Ted resin (Macherey-Nagel, Düren, Germany) using the elution buffer: 50 mM Tris, pH 7.2, 300 mM NaCl, 250 mM imidazole, 1 mM DTT, 0.1% CHAPS and protease inhibitor cocktail (#11873580001, Sigma). The protein was further purified by size exclusion chromatography (SEC) with a HiLoad 26/60 Superdex 200 pg column (GE Healthcare, Chicago, IL) in SEC buffer (50 mM Tris, pH 7.2, 300 mM NaCl, 1 mM DTT, 0.1% CHAPS) using an ÄKTA pure chromatography system (GE Healthcare). The protein was

concentrated with Amicon ultracentrifugal 3 K filter device (Millipore, Sigma, Burlington, MA). The homodispersity of the proteins was verified with SDS-PAGE.

**SPN-ARR domains of SHANK3**. The SPN-ARR fragment of rat SHANK3 (residues 1-348) was cloned into the pET-SUMO vector (Champion™ pET SUMO Protein Expression System, Invitrogen) to contain an N-terminal His6-SUMO tag. The protein was purified using nickel-affinity chromatography with a linear gradient containing 500 mM imidazole. The SUMO tag was cleaved with recombinant His-tagged SUMO protease and removed by a reverse pass on the Ni-NTA column. SHANK3 was shown to have >95% purity by SDS–PAGE gel.

### Microscale thermophoresis (MST)

The interaction between recombinant SHANK3 SPN and KRASG12V and SHANK3 SPN and E01 nanobody were measured using MST. His-SPN was labelled using the Monolith His-Tag Labelling Kit Red-tris-NTA fluorescent dye (Cat no. L008, NanoTemper Technologies) and applied at the final concentration of 50 nM in His-SPN SEC buffer having 0.05% Tween-20. A 12-point two-fold dilution series of unlabelled KRASG12V or E01 nanobody was mixed with labelled His-SPN protein and the indicated concentration ranges. MST experiments were conducted in triplicate using Monolith automated capillaries (Cat no. MO-AK002, NanoTemper Technologies) with a Monolith NT Automated system (NanoTemper Technologies) to determine the binding affinity between His-SPN and KRASG12V. The dissociation constant was then calculated using a single-site binding model to fit the curve using GraphPad Prism version 8.4.2 for Windows (GraphPad Software Inc.).

### Isothermal titration calorimetry (ITC)

For ITC measurements, the buffer of purified recombinant proteins (SPN-ARR fragment of SHANK3, GMPPCP-or GDP-loaded His6-KRASQ61H and RBD domain of *human* BRAF) was exchanged for ITC buffer (20 mM Tris pH 7.5, 500 mM NaCl, 0.5 mM TCEP (tris-carboxyethyl-phosphine) and 5 mM $MgCl_2$) and ITC experiments were performed using an ITC-200 (Microcal). Protein concentrations were estimated from UV absorbance at 280 nm. ITC titrations were performed at 25 °C using 20 μM of SHANK3 with 350 μM of KRASQ61H and 20 μM of KRASQ61H with 200 μM of RAF-RBD. Data were integrated and fitted to a single-site binding equation using Origin 7 software with an ITC module (Microcal).

### Atomistic simulation models and methods

To probe the spontaneous membrane-binding capabilities of SHANK3, simulations were performed within three different lipid bilayer systems. Spontaneously formed KRAS-membrane complexes were also analysed. Finally, the KRAS–SHANK3 complex was obtained by aligning the structures of SHANK3 SPN[35] to the RAF RBD[43] coordinates. To run the simulations, we used the GROMACS simulation package version 2020[68] and the CHARMM36m force field[69]. Every simulation system was inspected with four independent replicas. Total simulation sampling time was about 24 μs. The model systems and simulation parameters are described in detail below.

**SHANK3 with a lipid bilayer (Systems 1-3).** System S1 was comprised of SHANK3 SPN-ARR with a pure 1-palmitoyl-2-oleoyl-sn-glycero-3-phosphocholine (POPC) lipid bilayer. System S2 with SHANK3 SPN-ARR entails a symmetric three-component bilayer, containing 65 mol% POPC, 30 mol% cholesterol, and 5 mol% phosphatidylinositol 4,5-bisphosphate (PIP2). The SPN-ARR domain was initially placed about 2 nm away from the bilayer surface, with the SPN-ARR linker and the residues 105-115 of the ARR domain facing the bilayer. System S3 includes an isolated SPN domain (residues 2–93) together with the above-described three-component (POPC/cholesterol/PIP2) bilayer. The SPN domain was placed initially about 2 nm from the membrane surface. These constructs were based on the 5G4X structure[34]. Together these systems were used to probe spontaneous membrane binding capabilities of SHANK3. That is, the protein complex was initially placed in a random orientation such that the protein was allowed to bind the membrane without any bias, and these processes were simulated through four independent repeats (Supplementary Table 1). Hence, we refer to these systems as Spontaneous (see Supplementary Fig. 3).

**KRAS with a lipid bilayer (System S4)**. System S4 entailed KRAS in an initially soluble state and a POPC/cholesterol/PIP2 lipid bilayer. The protein coordinates were extracted from the PDB id 6PTW structure[43]. The resulting spontaneously formed KRAS-membrane complexes were analysed and compared to the known orientations in System S5 (see below). As in the previous case, System 4 was also studied through spontaneous binding.

**SHANK3 and KRAS with a lipid bilayer (System S5).** System S5 included a KRAS–SHANK3 SPN-ARR complex and a POPC/cholesterol/PIP2 lipid bilayer. The KRAS–SHANK3 complex was obtained by aligning the structures of SHANK3 SPN[34,35] to the RAF RBD coordinates extracted from the PDB id 6PTW[43]. The resulting KRAS–SHANK3 model was then equilibrated for 100 ns with 5 kJ/mol restraints on the backbone atoms. In this model, the (initial) protein-lipid configuration was extracted from the RAF RBD structure. Hence, we refer to these systems as Model (see Supplementary Fig. 3).

Simulations were initiated using the CHARMM-GUI portal[70,71]. Interactions between the atoms were described using the all-atom CHARMM36m force field[72]. Water molecules were described using the TIP3P water model[73]. Potassium and chloride ions were added to neutralise the charge of the systems and to reach the physiological saline concentration (150 mM).

**Simulation parameters**. To run the simulations, we used the GROMACS simulation package version 2020[68]. Initiation of the systems followed the general CHARMM-GUI protocol: the simulation systems were first energy-minimised and then equilibrated with position restraints acting on the solute atoms[72]. We used the leap-frog integrator with a timestep of 2 fs to propagate the simulations[74]. Periodic boundary conditions were applied in all three dimensions, atomic neighbours were tracked with the Verlet lists, and bonds were constrained with the LINCS algorithm[75]. Lennard-Jones interactions were cut off at 1.2 nm, while electrostatic interactions were calculated using the smooth particle mesh Ewald (PME) algorithm[76]. The pressure of the system was coupled semi-isotropically using the Parrinello-Rahman barostat with a time constant of 5 ps[76]. Protein, membrane, and solvent atoms were coupled separately with a time constraint of 1 ps. Simulation trajectories were saved every 100 ps. Random initial velocities were assigned for the atoms from the Boltzmann distribution at the beginning of each simulation. For the remaining parameters, we refer to the GROMACS 2020.2 defaults[68]. Production simulations are listed in Supplementary Table 1. The total simulation time of the atomistic simulations was >24 microseconds. In every system simulated, the first 100 ns were used for equilibration and were discarded from analysis. The analysis was performed for the remaining part of trajectories and over all four independent repeats/replicas (Supplementary Table 1). The error analysis, resulting in standard errors, was based on these data.

### Immunofluorescence

Cells were transfected as indicated and then fixed with 4% PFA in PBS for 10 min at room temperature and washed with PBS. For antibody staining, fixed cells were permeabilized with 0.5% Triton-X-100 in PBS for 10 min at room temperature and PFA was quenched with 1 M

glycine for 30 min at room temperature. For imaging ERK1/2, cells were stained with the primary antibody diluted in PBS (ERK1/2, 1:100, Cat. no. 91025, Cell Signalling) for 30 min at room temperature. Cells were washed 3 times with PBS and incubated with Alexa Fluor-conjugated secondary antibody (1:300, Life Technologies) and 4′6-diamidino-2-phenylindole (DAPI, nuclei staining, 1:10000; Cat. no. D1306, Life Technologies) diluted in PBS for 30 min at room temperature and then washed thrice with PBS. For imaging SHANK3, fixed and permeabilized cells were stained with anti-SHANK3 antibody (1:200 in PBS with 10% horse serum; SHANK3, Cat. no. HPA003446, Sigma-Aldrich) overnight at 4 °C before being washed 3 times with PBS and incubated with Alexa Flour-conjugated secondary antibody (1:500, Life Technologies) and Phalloidin-Atto 647 N (1:500, Sigma-Aldrich) for 1 h at room temperature. Cells were then washed 3 times with PBS and incubated with DAPI (1:10000) for 5 min at room temperature, and washed thrice with PBS.

For the ERK biosensor, PANC-1 ERK-KTR-mRuby2 cells were plated on glass-bottom dishes (Cat. no. P35G-1.5-20-C, MatTek Corporation) and silenced by siRNAs for two or three days, as described above. Then, cells were fixed with 4% PFA in PBS for 10 min at room temperature and washed with PBS.

Imaging was performed with a 3i spinning disk confocal (Marianas spinning disk imaging system with a Yokogawa CSU-W1 scanning unit on an inverted Carl Zeiss Axio Observer Z1 microscope, Intelligent Imaging Innovations, Inc.). To obtain a quantitative estimate for the extent of ERK nuclear translocation (indicative of ERK activity), captured images of cells were then analysed by calculating the ratio of staining intensity measured in the nucleus to that of a cytoplasmic region of the cell. This procedure accounts for potential variability in staining efficiency between different cell cultures.

### FRET imaging using fluorescence lifetime imaging microscopy (FLIM)

To visualise SHANK3–KRAS interaction in cells, we used FRET-FLIM. HEK293 cells were grown on coverslips overnight and transfected with an eGFP-tagged donor construct (GFP-SHANK3 SPN WT or GFP-SHANK3 SPN R12E/K22D) and mCherry-tagged acceptor construct (mCherry-KRASG12V). For the donor fluorophore-only samples, 0.8 μg GFP SHANK3 SPN WT or R12E/K22D mutant was used. For the donor-acceptor FRET pairs, cells were transfected with one of the donor plasmids and mCherry-KRASG12V as the acceptor (mCherry-C1 for control) at a construct ratio of 1: 3 (donor: acceptor). Media was changed 5 h after transfection. 48 h post-transfection, cells were fixed with 4% PFA/PBS and mounted in Mowiol 4-88 on microscope slides. Fluorescence lifetimes of the GFP-tagged donor constructs were measured using a fluorescence lifetime imaging attachment (Lambert Instruments, Leutingwolde, The Netherlands) on an inverted microscope (Zeiss Axio Observer.D1). Fluorescein (0.01 mM, pH 9) was used as a lifetime reference standard. The apparent FRET efficiency (Eapp) was calculated as the percentage of each donor-acceptor pair (τDA) and the average lifetime of the donor only (τD) samples ($Eapp = (1 - \tau DA/\tau D) \times 100\%$)[44]. Apparent FRET efficiency values were normalized to the average of the replicate 1 mCherry control. To analyse SHANK3 regulation of effector recruitment, HEK293 cells were first silenced with control or *SHANK3*-targeting siRNA for 48 h, and then, seeded on a 6-well plate with glass coverslips, and transfected with the donor alone plasmid (mGFP-tagged KRASG12V construct) in control samples, or with the donor plasmid and the acceptor plasmid mRFP-RBD in CRAF-RBD-recruitment FRET experiments. After 48 h of plasmid transfection, coverslips were fixed with 4% PFA/PBS for 15 min and then washed with PBS, and coverslips were mounted with Mowiol 4–88 (Sigma-Aldrich) on microscope slides.

### In vivo chick embryo chorioallantoic membrane (CAM) assay

The shells of fertilised chicken eggs were cleaned with 70% ethanol prior to starting development, before placing the eggs in a humidified incubator (50% moisture, 37 °C). On day 3 of development, a small hole was made with a needle and tweezers in the eggshell to drop the CAM away from the shell. On developmental day 7, the hole was widened with tweezers in order to place a plastic ring on the CAM. One million cells (transiently transfected with plasmids or siRNAs) were implanted inside the ring in 20 μl of 50% Matrigel (Cat. no. 354230, Corning) diluted in PBS, after which the hole was covered with parafilm to avoid drying of the CAM. The tumours were harvested 4–5 days post-implantation by placing the eggs on ice for 30 min before dissecting, weighing and fixing the tumours in 10% PBS (pH 7; Cat. no. FFCHFF1195000, VWR).

### Subcutaneous tumour xenografts in Nude mice

To evaluate the requirement for SHANK3 in established tumours, six- to eight-week-old female athymic Nude mice (Hsd:Athymic Nude-foxn1nu, Envigo, France) were injected in the flank with 5 million PANC-1 cells, expressing dox-inducible *SHANK3* shRNA (pool of clones 4 S and 1 C), resuspended in 100 μl PBS with 50% Matrigel (Cat. no. 354230, Corning). When tumours reached an average mean volume of 100 $mm^3$, the mice with similarly sized tumours were blindly randomised into two cohorts. Then, mice were fed either a normal chow (control group; Teklad 2914 diet, Envigo) or dox-containing chow (*SHANK3*-depleted group; Teklad doxycycline-diet, 625 mg/kg, in 2014 diet base, irradiated (2914), colour red, Envigo) daily. In addition, mice received two intraperitoneal (i.p) injections of PBS or doxycycline (80 mg/kg of body weight) according to their treatment group on day 1 and 2 of dox induction. Successful induction of *SHANK3* shRNA expression (tRFP expression after dox-induction) was confirmed by imaging on an IVIS spectrum (PerkinElmer) and the radiant efficiency calculated by the IVIS software. Tumours were measured with a digital calibre twice a week and tumour volumes were calculated according to the formula $V = (\pi/6)(d1 \times d2)\ \hat{}\ 3/2$, where d1 and d2 are perpendicular tumour diameters. Mice were sacrificed at 26 days post-induction (74 post-engraftment), and tumours were dissected, weighed and snap-frozen in liquid nitrogen for mRNA isolation.

All animal experiments were ethically assessed and authorised by the National Animal Experiment Board and in accordance with The Finnish Act on Animal Experimentation (Animal license numbers ESAVI/9339/2016 and ESAVI/37571/2019). Mice were housed in standard conditions (12 h light/dark cycle) with food (as indicated above) and water available ad libitum, and randomly assigned to experimental groups. All experiments respected the maximum tumour diameter (15 mm) permitted by the authorisation bodies.

### Immunohistochemistry analysis of tumours

Formalin-fixed, paraffin-embedded tissue samples were cut to 4 μm sections, deparaffinised and rehydrated with standard procedures. For immunohistochemistry (IHC) of CAM tumours, heat-mediated antigen retrieval was done in citrate buffer (pH 6 for cleaved caspase-3, pH 9 for Ki-67). Sections were washed with washing buffer (0.05 M Tris-HCl pH 7.6, 0.05% Tween20), blocked for endogenous hydrogen peroxide activity, and incubated with Normal Antibody Diluent (NABD; Cat. No. BD09-125, Immunologic). Sections were then incubated with a Ki-67 antibody (Cat. no. AB9260, Millipore, diluted 1:1000) or a Cleaved Caspase-3 (Asp175) antibody (Cat. no. 9664, clone 5A1E, Cell Signalling Technology, diluted 1:500) for 1 h. The samples were washed thrice with TBS, incubated for 30 min with a BrightVision Goat anti-Rabbit HRP (Cat. no. DPVR110HRP, Immunologic) secondary antibody and washed again with TBS. DAB solution (Cat. no. K3468, DAKO) was added for 10 s followed by washing thrice with TBS. After counter-staining with Mayer's HTX, slides were dehydrated, and cleared in xylene, and mounted in Pertex. Stained samples were imaged with

Pannoramic P1000 Slide Scanner (3DHISTECH Ltd) and analysed with QuantCenter software using the NuclearQuant quantification module (3DHISTECH Ltd).

### Production of recombinant anti-SHANK3 SPN nanobodies

**Nanobody generation**. Nanobodies (single domain antibodies) against SHANK3 SPN were produced by Hybrigenics Services SAS (Evry, France; www.hybribody.com) by three rounds of Phage Display selection of their naïve VHH-library against recombinant biotinylated GST-SHANK3 SPN protein as briefly described below.

Prior to the Phage Display selection, SPN-Biotin and a non-related protein, GST-HIS-MBP-FLAG-Biotin, were bound to Streptavidin Magnetic Beads (Dynabeads® M-280 Streptavidin, Life Technologies) at a final concentration of 50 nM (1st round) and 10 nM (2nd and 3rd rounds).

For phage display selection, unspecific binders were first removed from the hs2dAb Phage Display library by incubation with the GST-HIS-MBP-FLAG-Biotin beads. Then, the unbound VHHs expressed as an *E. coli* supernatant were incubated with the SPN-Biotin beads and a total of three rounds of Phage Display were performed. The depletion step was repeated before each round of Phage Display to remove non-specific VHHs. At the end of the third round of Phage Display, *E. coli* clones were analysed by Hybrigenics' non-adsorbed phage ELISA, which allows for the proper folding of the native SPN protein, in 384-well plates with HRP-conjugated anti- M13 antibody (GE Healthcare) and a colorimetric substrate (TMB, TetraMethylBenzidine, Thermo Fischer). VHH clones with a significant ELISA signal in the presence of SPN-Biotin and a very low signal in the presence of GST-HIS-MBP-FLAG-Biotin were considered as specific SPN binders and selected for sequence analysis. Sequencing revealed that all binders represented one of two VHH variants (hereafter called nanobodies A01 and E01). These were provided by Hybrigenics in the bacterial expression vector pHEN2 (C-terminal 6xHis and 3 Myc tags) for use in ELISA assays and in in vitro pulldowns, and in an mCherry mammalian expression vector (tag on C terminus) for use in cell-based assays. A single-chain variable fragment (scFv) against an unrelated protein (SorLA) was used as a negative control in ELISA assays.

**Recombinant nanobody production.** Nanobodies in the pHEN2 vector were produced as recombinant proteins in BL21 bacteria using IPTG induction and purified according to Hybrigenics' protocol. Briefly, transformed bacteria were cultured overnight in TB medium (2.4% w/v yeast extract, 1.2% w/v tryptone, 0.4% w/v glycerol, 0.017 M KH2PO4, 0.072 M K2HPO4, 1% glucose, 100 μg/ml ampicillin) at 37 °C. 2 ml of this starter culture were then reincubated at 37 °C until optical density at 600 nm was between 0.6 and 0.8, induced with IPTG (0.5 mM) overnight at 28 °C, pelleted and freeze-thawed in liquid nitrogen. The pellet was resuspended in sonication buffer (50 mM $NaPO_4$, pH 8, 300 mM NaCl, bacterial protease inhibitors, 1 mM PMSF, 1 mg/ml lysozyme), sonicated on ice (3 times for 1 s) and centrifuged to remove debris. Lysates were then incubated with prewashed Talon metal affinity resin (BD) at 4 °C for 30 min with shaking. Resin was then spun, flow-through removed, and washed with sonication buffer. Nanobodies were then eluted in sonication buffer plus 250 mM imidazole.

### Functional ELISA assay for nanobody testing

Nunc maxisorp 96-well plates were coated with 5 μg/ml purified recombinant His-SHANK3 SPN protein in TBS, 100 μl/well, overnight at 4 °C. Wells coated with BSA alone were included as a background binding control. The coating solution was removed, the wells were blocked with 100 μl/well 5% BSA in TBS-0.1% Tween20 (TBST) for 1 h at room temperature. The His-SPN coated wells were preincubated with the nanobodies for 15 min at room temperature prior to addition of GST-tagged purified recombinant KRAS protein loaded with non-hydrolysable GTP analogue. An irrelevant anti-SorLA single-chain antibody (sc-Fv) was added as a negative control. These were incubated for 1 h at room temperature in TBST + 1 mM DTT + 2 mM $MgCl_2$. Wells were washed 3 times with TBST + 2 mM $MgCl_2$. To detect GST, DELFIA® Eu-N1 Anti-GST antibody (Perkin Elmer catalogue number AD0250) diluted at 1:000 in TBST + 1 mM DTT + 2 mM $MgCl_2$ was added and incubated 1 h at room temperature. The wells were washed thrice with Tecan plate washer with PBS, 100 μl of DELFIA® Enhancement Solution (Perkin Elmer catalogue number 124-105) was added to the wells and europium signal was measured with a time resolved fluorescence plate reader (PerkinElmer's VICTOR X5 multilabel plate reader).

### Pull-down interaction assay

The ability of anti-SHANK3 SPN nanobodies (A01 and E01) to disrupt the interaction between SHANK3 SPN and KRASG12V was tested with a pull-down. 5 μg of His-SHANK3 SPN protein was bound to 20 μl of Macherey Nagel Protino Ni-Ted resin beads in TBS + 1 mM DTT + 2 mM $MgCl_2$ for 1 h under rotation at 4 °C. 20 μg of nanobodies A01 or E01 or BSA as control were incubated with this for 30 min under rotation at 4 °C. 5 μg/ml GST-KRAS-GTP or GST alone was added and incubated under rotation at 4 °C for 1 h. Beads were washed thrice with 500 μl TBS + 1 mM DTT + 2 mM $MgCl_2$, eluted into 20 μl 4x SDS sample buffer (200 mM Tris-HCl pH 6.8, 8% SDS, 40% glycerol, 4% β-mercaptoethanol, 50 mM EDTA, 0.08% bromophenol blue) with heating at 90 °C for 5 min and separated on an SDS-PAGE gel. The proteins were transferred to a filter and western blotted with anti-GST antibody.

### Statistics and Reproducibility

The sample size for studies was chosen according to previous studies in the same area of research. The GraphPad program was used for all statistical analyses. Normal distribution of the data was tested with the D'Agostino & Pearson omnibus normality test. Student's *t*-test (unpaired, two-tailed) with Welch's correction was used for two groups when normality could be confirmed. Nonparametric Mann–Whitney U-test was used when two non-normally distributed groups were compared or when normality could not be tested [due to a too small data set ($n < 8$)]. ANOVA with Holm-Sidak's or Dunnett's multiple comparison test was used when comparing more than two normally distributed groups. The Kruskal-Wallis non-parametric test with Dunn's multiple comparison test was used when comparing more than two non-normally distributed groups. Data are presented in column graphs or scatter dot plots with mean ± standard error of the mean (s.e.m) or mean ± standard deviation (s.d) and *P*-values. Individual data points per condition are shown, and *n*-numbers are indicated in the figure legends. The graphs in Figs. 2g and 3g were generated using SuperPlotsofData[77] and all data points and the average of each biological replicate are shown. *P*-values less than 0.05 were considered to be statistically significant. Unless otherwise indicated, all micrographs (western blots and microscopy images) are representative of three or more independent experiments (*n* numbers are shown in the accompanying analyses for each micrograph). The original, uncropped western blots can be found in the Source Data file.

### Reporting summary

Further information on research design is available in the Nature Portfolio Reporting Summary linked to this article.

## Data availability

The authors declare that the data supporting the findings of this study are available within the paper and its supplementary information files. Source data are provided with this paper.

## Code availability

The molecular dynamics simulation files generated and analyzed during the current study are available in the Zenodo repository,

accessible at https://doi.org/10.5281/zenodo.5541745. These files include the initial structures, input files, and trajectory files.

## References


1. Prior, I. A., Hood, F. E. & Hartley, J. L. The frequency of ras mutations in cancer. *Cancer Res.* **80**, 2969–2974 (2020).
2. Simanshu, D. K., Nissley, D. V. & McCormick, F. RAS proteins and their regulators in human disease. *Cell* **170**, 17–33 (2017).
3. DeStefanis, R. A., Kratz, J. D., Emmerich, P. B. & Deming, D. A. Targeted therapy in metastatic colorectal cancer: current standards and novel agents in review. *Curr. Colorectal Cancer Rep.* **15**, 61–69 (2019).
4. Waters, A. M. & Der, C. J. KRAS: The critical driver and therapeutic target for pancreatic cancer. *Cold Spring Harb. Perspect. Med.* **8**, a031435 (2018).
5. Salgia, R., Pharaon, R., Mambetsariev, I., Nam, A. & Sattler, M. The improbable targeted therapy: KRAS as an emerging target in non-small cell lung cancer (NSCLC). *Cell Rep. Med.* **2**, 100186 (2021).
6. Siegel, R. L., Miller, K. D., Fuchs, H. E. & Jemal, A. Cancer Statistics, 2021. *CA Cancer J. Clin.* **71**, 7–33 (2021).
7. Vetter, I. R. & Wittinghofer, A. The guanine nucleotide-binding switch in three dimensions. *Science* **294**, 1299–1304 (2001).
8. Cox, A. D. & Der, C. J. Ras history: the saga continues. *Small GTPases* **1**, 2–27 (2010).
9. Drosten, M. & Barbacid, M. Targeting the MAPK pathway in KRAS-driven tumors. *Cancer Cell* **37**, 543–550 (2020).
10. Stalnecker, C. A. & Der, C. J. RAS, wanted dead or alive: advances in targeting RAS mutant cancers. *Sci. Signal* **13**, eaay6013 (2020).
11. Ostrem, J. M., Peters, U., Sos, M. L., Wells, J. A. & Shokat, K. M. K-Ras(G12C) inhibitors allosterically control GTP affinity and effector interactions. *Nature* **503**, 548–551 (2013).
12. Fell, J. B. et al. Identification of the clinical development candidate MRTX849, a covalent KRASG12C inhibitor for the treatment of cancer. *J. Med. Chem.* **63**, 6679–6693 (2020).
13. Hong, D. S. et al. KRASG12C inhibition with sotorasib in advanced solid tumors. *N. Engl. J. Med.* **383**, 1207–1217 (2020).
14. Canon, J. et al. The clinical KRAS(G12C) inhibitor AMG 510 drives anti-tumour immunity. *Nature* **575**, 217–223 (2019).
15. Lanman, B. A. et al. Discovery of a covalent Inhibitor of KRASG12C (AMG 510) for the treatment of solid tumors. *J. Med. Chem.* **63**, 52–65 (2020).
16. Janes, M. R. et al. Targeting KRAS mutant cancers with a covalent G12C-specific inhibitor. *Cell* **172**, 578–589.e17 (2018).
17. Mao, Z. et al. KRAS(G12D) can be targeted by potent inhibitors via formation of salt bridge. *Cell Discov.* **8**, 5 (2022).
18. Zhang, Z. et al. GTP-state-selective cyclic peptide ligands of K-ras(G12D) block its interaction with Raf. *ACS Cent. Sci.* **6**, 1753–1761 (2020).
19. Molina-Arcas, M., Samani, A. & Downward, J. Drugging the undruggable: advances on RAS targeting in cancer. *Genes (Basel)* **12**, 899 (2021).
20. Di Nicolantonio, F. et al. Precision oncology in metastatic colorectal cancer - from biology to medicine. *Nat. Rev. Clin. Oncol.* **18**, 506–525 (2021).
21. Awad, M. M. et al. Acquired resistance to KRASG12C inhibition in cancer. *N. Engl. J. Med.* **384**, 2382–2393 (2021).
22. Tanaka, N. et al. Clinical acquired resistance to KRASG12C inhibition through a novel KRAS switch-II pocket mutation and polyclonal alterations converging on RAS-MAPK reactivation. *Cancer Discov.* **11**, 1913–1922 (2021).
23. Zhao, Y. et al. Diverse alterations associated with resistance to KRAS(G12C) inhibition. *Nature* **599**, 679–683 (2021).
24. Hofmann, M. H., Gerlach, D., Misale, S., Petronczki, M. & Kraut, N. Expanding the reach of precision oncology by drugging All KRAS mutants. *Cancer Discov.* **12**, 924–937 (2022).
25. Kim, D. et al. Pan-KRAS inhibitor disables oncogenic signalling and tumour growth. *Nature* **619**, 160–166 (2023).
26. Hofmann, M. H. et al. BI-3406, a potent and selective SOS1-KRAS interaction inhibitor, is effective in KRAS-driven cancers through combined MEK inhibition. *Cancer Discov.* **11**, 142–157 (2021).
27. Kerr, D. L., Haderk, F. & Bivona, T. G. Allosteric SHP2 inhibitors in cancer: targeting the intersection of RAS, resistance, and the immune microenvironment. *Curr. Opin. Chem. Biol.* **62**, 1–12 (2021).
28. Nichols, R. J. et al. RAS nucleotide cycling underlies the SHP2 phosphatase dependence of mutant BRAF-, NF1- and RAS-driven cancers. *Nat. Cell Biol.* **20**, 1064–1073 (2018).
29. Bery, N., Miller, A. & Rabbitts, T. A potent KRAS macromolecule degrader specifically targeting tumours with mutant KRAS. *Nat. Commun.* **11**, 3233 (2020).
30. Gutierrez-Prat, N. et al. DUSP4 protects BRAF- and NRAS-mutant melanoma from oncogene overdose through modulation of MITF. *Life Sci. Alliance* **5**, e202101235 (2022).
31. Ito, T. et al. Paralog knockout profiling identifies DUSP4 and DUSP6 as a digenic dependence in MAPK pathway-driven cancers. *Nat. Genet* **53**, 1664–1672 (2021).
32. Leung, G. P. et al. Hyperactivation of MAPK Signaling Is Deleterious to RAS/RAF-mutant Melanoma. *Mol. Cancer Res.* **17**, 199–211 (2019).
33. Chang, L. et al. Systematic profiling of conditional pathway activation identifies context-dependent synthetic lethalities. *Nat. Genet* **55**, 1709–1720 (2023).
34. Lilja, J. et al. SHANK proteins limit integrin activation by directly interacting with Rap1 and R-Ras. *Nat. Cell Biol.* **19**, 292–305 (2017).
35. Cai, Q., Hosokawa, T., Zeng, M., Hayashi, Y. & Zhang, M. Shank3 binds to and stabilizes the active form of Rap1 and HRas GTPases via its NTD-ANK tandem with distinct mechanisms. *Structure* **28**, 290–300.e4 (2020).
36. Sheng, M. & Kim, E. The Shank family of scaffold proteins. *J. Cell Sci.* **113**, 1851–1856 (2000).
37. Salomaa, S. I. et al. SHANK3 conformation regulates direct actin binding and crosstalk with Rap1 signaling. *Curr. Biol.* **31**, 4956–4970.e9 (2021).
38. Dempster, J. M. et al. Agreement between two large pan-cancer CRISPR-Cas9 gene dependency data sets. *Nat. Commun.* **10**, 5817 (2019).
39. Cowley, G. S. et al. Parallel genome-scale loss of function screens in 216 cancer cell lines for the identification of context-specific genetic dependencies. *Sci. Data* **1**, 140035 (2014).
40. Rezaei Adariani, S. et al. A comprehensive analysis of RAS-effector interactions reveals interaction hotspots and new binding partners. *J. Biol. Chem.* **296**, 100626 (2021).
41. Nassar, N. et al. Ras/Rap effector specificity determined by charge reversal. *Nat. Struct. Biol.* **3**, 723–729 (1996).
42. Hancock, J. F., Paterson, H. & Marshall, C. J. A polybasic domain or palmitoylation is required in addition to the CAAX motif to localize p21ras to the plasma membrane. *Cell* **63**, 133–139 (1990).
43. Fang, Z. et al. Multivalent assembly of KRAS with the RAS-binding and cysteine-rich domains of CRAF on the membrane. *Proc. Natl Acad. Sci. USA* **117**, 12101–12108 (2020).
44. Guzmán, C. et al. The efficacy of raf kinase recruitment to the GTPase H-ras depends on H-ras membrane conformer-specific nanoclustering. *J. Biol. Chem.* **289**, 9519–9533 (2014).
45. Unni, A. M. et al. Hyperactivation of ERK by multiple mechanisms is toxic to RTK-RAS mutation-driven lung adenocarcinoma cells. *Elife* **7**, e33718 (2018).
46. Cho, E., Lou, H. J., Kuruvilla, L., Calderwood, D. A. & Turk, B. E. PPP6C negatively regulates oncogenic ERK signaling through dephosphorylation of MEK. *Cell Rep.* **34**, 108928 (2021).
47. Timofeev, O., Giron, P., Lawo, S., Pichler, M. & Noeparast, M. ERK pathway agonism for cancer therapy: evidence, insights, and a target discovery framework. *npj Precis. Onc.* **8**, 1–16 (2024).

48. Kudo, T. et al. Live-cell measurements of kinase activity in single cells using translocation reporters. *Nat. Protoc.* **13**, 155–169 (2018).
49. Wang, L. et al. A kinome-wide RNAi screen identifies ERK2 as a druggable regulator of Shank3 stability. *Mol. Psychiatry* **25**, 2504–2516 (2020).
50. Hayes, T. K. et al. Long-term ERK inhibition in KRAS-mutant pancreatic cancer is associated with MYC degradation and senescence-like growth suppression. *Cancer Cell* **29**, 75–89 (2016).
51. Dias, M. H. & Bernards, R. Playing cancer at its own game: activating mitogenic signaling as a paradoxical intervention. *Mol. Oncol.* **15**, 1975–1985 (2021).
52. Wood, K. C. Hyperactivation of oncogenic driver pathways as a precision therapeutic strategy. *Nat. Genet.* **55**, 1613–1614 (2023).
53. Nakajima, E. C. et al. FDA approval summary: sotorasib for KRAS G12C-mutated metastatic NSCLC. *Clin. Cancer Res.* **28**, 1482–1486 (2022).
54. Jovčevska, I. & Muyldermans, S. The therapeutic potential of nanobodies. *BioDrugs* **34**, 11–26 (2020).
55. Jameson, K. L. et al. IQGAP1 scaffold-kinase interaction blockade selectively targets RAS-MAP kinase-driven tumors. *Nat. Med.* **19**, 626–630 (2013).
56. Diepstraten, S. T. et al. The manipulation of apoptosis for cancer therapy using BH3-mimetic drugs. *Nat. Rev. Cancer* **22**, 45–64 (2022).
57. Ledford, H. Gene-silencing technology gets first drug approval after 20 year wait. *Nature* **560**, 291–292 (2018).
58. Honor, A., Rudnick, S. R. & Bonkovsky, H. L. Givosiran to treat acute porphyria. *Drugs Today (Barc.)* **57**, 47–59 (2021).
59. Shah, V. N. & Pyle, L. Lumasiran, an RNAi therapeutic for primary hyperoxaluria type 1. *N. Engl. J. Med.* **385**, e69 (2021).
60. Kreienkamp, H.-J. Scaffolding proteins at the postsynaptic density: shank as the architectural framework. *Handb Exp. Pharmacol.* **186**, 365–380 (2008).
61. Abankwa, D. et al. A novel switch region regulates H-ras membrane orientation and signal output. *EMBO J.* **27**, 727–735 (2008).
62. Najumudeen, A. K. et al. Cancer stem cell drugs target K-ras signaling in a stemness context. *Oncogene* **35**, 5248–5262 (2016).
63. Vuoriluoto, K. et al. Vimentin regulates EMT induction by slug and oncogenic H-Ras and migration by governing Axl expression in breast cancer. *Oncogene* **30**, 1436–1448 (2011).
64. Härmä, V. et al. A comprehensive panel of three-dimensional models for studies of prostate cancer growth, invasion and drug responses. *PLoS ONE* **5**, e10431 (2010).
65. Guzmán, C., Bagga, M., Kaur, A., Westermarck, J. & Abankwa, D. ColonyArea: an ImageJ plugin to automatically quantify colony formation in clonogenic assays. *PLoS ONE* **9**, e92444 (2014).
66. Schindelin, J. et al. Fiji: an open-source platform for biological-image analysis. *Nat. Methods* **9**, 676–682 (2012).
67. John, J. et al. Kinetics of interaction of nucleotides with nucleotide-free H-ras p21. *Biochemistry* **29**, 6058–6065 (1990).
68. Abraham, M. J. et al. GROMACS: High performance molecular simulations through multi-level parallelism from laptops to supercomputers. *SoftwareX* **1–2**, 19–25 (2015).
69. Huang, J. et al. CHARMM36m: an improved force field for folded and intrinsically disordered proteins. *Nat. Methods* **14**, 71–73 (2017).
70. Jo, S., Kim, T., Iyer, V. G. & Im, W. CHARMM-GUI: a web-based graphical user interface for CHARMM. *J. Comput. Chem.* **29**, 1859–1865 (2008).
71. Wu, E. L. et al. CHARMM-GUI membrane builder toward realistic biological membrane simulations. *J. Comput. Chem.* **35**, 1997–2004 (2014).
72. Lee, J. et al. CHARMM-GUI input generator for NAMD, GROMACS, AMBER, OpenMM, and CHARMM/OpenMM simulations using the CHARMM36 additive force field. *J. Chem. Theory Comput.* **12**, 405–413 (2016).
73. Mark, P. & Nilsson, L. Structure and dynamics of the TIP3P, SPC, and SPC/E water models at 298. *K. J. Phys. Chem. A* **105**, 9954–9960 (2001).
74. Van Gunsteren, W. F. & Berendsen, H. J. C. A leap-frog algorithm for stochastic dynamics. *Mol. Simul.* **1**, 173–185 (1988).
75. Hess, B., Bekker, H., Berendsen, H. J. C. & Fraaije, J. G. E. M. LINCS: A linear constraint solver for molecular simulations. *J. Comput. Chem.* **18**, 1463–1472 (1997).
76. Parrinello, M. & Rahman, A. Polymorphic transitions in single crystals: a new molecular dynamics method. *J. Appl. Phys.* **52**, 7182–7190 (1981).
77. Goedhart, J. SuperPlotsOfData-a web app for the transparent display and quantitative comparison of continuous data from different conditions. *Mol. Biol. Cell* **32**, 470–474 (2021).


## Acknowledgements

We thank P. Laasola, J. Siivonen, E-M. Vesilahti, M. Miihkinen, S. Salomaa and A. Isomursu for technical assistance and scientific discussion, the Ivaska lab for critical reading and feedback on the manuscript and O. Pentikäinen for protein complex modelling. The Cell Imaging and Cytometry Core (Turku Bioscience Centre, University of Turku) and Turku Centre for Disease Modelling (TCDM), both supported by Biocenter Finland, the Euro-BioImaging Finnish Node (Turku Finland), the University of Turku Histocore and Genome Editing core are acknowledged for services, instrumentation, and expertise. We also gratefully acknowledge CSC – IT Center for Science (Espoo, Finland) for providing ample computing resources. This work was supported by the Research Council of Finland through the following programs: an InFLAMES Flagship Programme (337530, UTU and 337531, Åbo Akademi), Research project grants (325464, J.I., and 331349, I.V.), Research Fellowships (338537 G.J. and 323096 E.P.), the CoE for Biological Barrier Mechanics and Disease (346131 & 364182, J.I., and 346135 & 364185, I.V.,). Additional funding was provided by an ERC consolidator (615258, J.I.) and a proof of concept grant (899155, J.I.), the Sigrid Juselius Foundation (J.I., G.J., E.P., and I.V.), the Finnish Cultural Foundation (J.L. and E.P), the Cancer Foundation Finland (J.I., M.S., G.J., and I.V.), the Frontier Science Program (RGP0059/2019, I.V.), the Helsinki Institute of Life Science (HiLIFE) Fellow program (I.V.), the Lundbeck Foundation (I.V.) and a Novo Nordisk pre-seed grant (J.I.). J.L., and J.K., were supported by the Turku Doctoral Programme of Molecular Medicine (TuDMM), J.L by the Instrumentarium Foundation, the Orion Research Foundation Sr and the K. Albin Johansson Foundation, and P.R. by the Drug Research Doctoral Programme at the University of Turku. J.R.W.C. was supported by the European Union's Horizon 2020 research and innovation programme under the Marie Sklodowska-Curie grant agreement [841973] and a Research Council of Finland postdoctoral research grant (338585), M.D. by the European Union's Horizon Europe research and innovation programme under Marie Sklodowska-Curie grant [101108089], M.C. by a Research Council of Finland postdoctoral research grant (343239) and AKN by CRUK Scotland Institute core funding (A17196, and A31287 - awarded to O.J.S.,). O.J.S., was supported by CRUK grants (A21139, A12481, A17196 and A31287) and an ERC Starting grant (311301).

## Author contributions

Conceptualization: J.L., J.I. Methodology: J.L., J.K, J.R.W.C., U.P., I.B., J.V., M.R.C., M.D., D.A., I.V., E.P., J.I. Formal Analysis: J.L., J.K., U.P., I.B., J.V., E.P., H.P. Investigation, J.L., J.K., H.P., T.V., G.J., E.P., M.R.C., M.D., J.V., P.R., I..M.D.P., E.W., A.K.N. Visualization: J.L., J.V., H.H. Writing – Original Draft: J.L., M.S., J.I. Writing – review & editing: J.L., J.K, H.H., J.R.W.C., G.J., E.P., A.K.N., O.J.S., D.A., J.V., I.V., M.S., J.I. Supervision: O.J.S., I.B., I.V., D.A., U.P., J.I. Funding Acquisition: I.V., J.I.

## Competing interests

The authors J.L. and J.I. declare that they have filed patent applications related to these findings (Therapy of Ras-Dependent Cancers, WO/2021/

160937; Nanobodies specifically binding to SH3 and multiple ankyrin repeat domains 3 (SHANK3), WO/2023/021181). All other authors declare no competing interests.

## Additional information

**Supplementary information** The online version contains supplementary material available at https://doi.org/10.1038/s41467-024-52326-1.

**Correspondence** and requests for materials should be addressed to Johanna Ivaska.

**Peer review information** *Nature Communications* thanks Mark Philips and the other, anonymous, reviewer(s) for their contribution to the peer review of this work. A peer review file is available.